Doping of Group IV Semiconductor Nanowires

Alexander Game, BSc

Masters of Research

University College Cork, Ireland

School of Chemistry

Head of School: Dr Humphrey Moynihan

Supervisor: Prof Justin Holmes

March 2020

Table of Contents

Declaration

This is to certify that the work I am submitting is my own and has not been submitted for another degree, either at University College Cork or elsewhere. All external references and sources are clearly acknowledged and identified within the contents. I have read and understood the regulations of University College Cork concerning plagiarism.

For my Mum and Dad, and my love, Ruthanna.

Thank you for all your love, encouragement, and support.

List of Abbreviations

Allyldiphenylphosphine (ADPP)

Allyltributylstannane (ATBS)

Aluminium (Al)

Antomony (Sb)

Arsenic (As)

Atomic Force Microscopy (AFM)

Atomic Probe Tomography (APT)

Bismuth (Bi)

Boron (B)

Chemical Vapour Deposition (CVD)

Diborane (B_2H_6)

Diphenylgermane (DPG)

Diphenylphosphine (DPP)

Electron Spin Resonance (ESR)

Electron-Beam Lithography (EBL)

Energy-Dispersive X-ray Spectroscopy(EDX)

Field-Effect Transistor (FET)

Galium Arsenide (GaAs)

Germanium (Ge)

Germanium dioxide (GeO_2)

Germanium-Tin (GeSn)

Gold (Au)

High resolution Transmission electron microscopy (HRTEM)

Hydrobromic Acid (HBr)

Hydrogen Chloride (HCl)

Ion-Beam Lithography (IBL)

Isopropanol (IPA)

Juntionless Nanowire Transistor (JNT)

Metal Oxide semiconductor Field Effect Transistor (MOSFET)

Metal-oxide Vapour-phase Epitaxy (MOVPE)

Monolayer Contact Doping (MLCD)

Monolayer Doping (MLD)

Multi-gate Field-Effect Transistor (MuGFET)

Nanoimprint Lithography (NIL)

Nanoparticle (NP)

Nanowire (NW)

Palladium (Pd)

Phosphine Gas (PH_3)

Phosphorus (P)

Scanning electron microscopy (SEM)

Scanning Transmission Electron Microscopy (STEM)

Silane (SiH_4)

Silicon (Si)

Silicon Dioxide (SiO2)

Silicon-on-insulator (SOI)

Silver (Ag)

Spin-on-doping (SOD)

Supercritical-fluid-liquid-solid (SFLS)

Titanium (Ti)

Transmission electron microscopy (TEM)

Trioctylphosphine (TOP)

Tunnel Field Effect Transistor (tFET)

Vapour-Liquid-Solid (VLS)

Vapour-Solid-Solid (VSS)

X-ray Diffraction (XRD)

Acknowledgements

Firstly, my thanks go to Prof. Justin Holmes for both the opportunity to partake in this research, and his consistent support, supervision and advise throughout the project. Without him, none of the research presented here would have been possible. I would also like to thank Dr John O'Connell and Dr Subhajit Biswas for all of their guidance and advise over the past few years. Also, to all of my colleagues in lab 115 and 320, past and present; thank you so very much for making all of the darker days much more bearable and bright, and for all of the laughs over the years. I cannot thank the technical and administrative staff in the school of chemistry enough, especially to Dr Trevor Carey and Dr Ian O'Connor for all of their assistance. Thanks are also due to my dear friend, Nathan Jeffers, not only for his assistance with the programming used in this thesis, but his ever present support, warmth and dear friendship. Special thanks to Shane Garvey, Tim Bourke, Will Daly and Eilís Ní Thuama, for all of their friendship, support and lunches. I could not have asked for a better group of friends, and 12:30 will never be the same again. Finally, the three people in my life who are dearest; David and Carolyn Game, and Ruthanna Stockhoff. Words cannot express how grateful I am to have been blessed with such amazing parents, and such a wonderful partner to share my life with. Your support, patience, counsel and love have been invaluable. Thank you so very much.

Abstract

As Moore's Law predicted in the 1960s, advancements in technology have led to an exponential increase in the numbers of transistors required per square inch of integrated circuits, leading to an ever pressing need for smaller transistors. In turn, there is a need for novel transistor architectures and materials, with the conventional Si FETs soon approaching the limits of modern technology. With the need for channel lengths and widths below 7 nm fast approaching, much research has turned to new materials and devices to fulfil these requirements when they are needed.

With NWs being prominently used in studies of alternative device architectures, and a resurgence in research of Ge as a semiconductor for FET channels, Ge NWs show great promise as components for novel FET designs. GeSn also shows great potential over Si and Ge due to its direct bandgap allowing for lower energy devices. While most reported syntheses of Ge NWs use gas-based vapour-liquid-solid growths, some research has been reported on solution-based VLS growth of both Ge and Ge Sn NWs, although no literature to date has reported solution-based doping of VLS grown Ge or GeSn NWs.

This thesis reports liquid-phase VLS growth and *in-situ* doping of Ge and GeSn NWs using a variety of dopant precursors. SEM and TEM were used to analyse the morphology of NWs grown. TEM, XRD and Raman Spectroscopy were used to analyse the crystal structures of the wires, including the presence of defects. Raman spectroscopy and EDX analysis were used to determine the atomic composition of the NWs. Electrical testing was also carried out on the NWs.

Chapter 1 of this thesis outlines the advantages of the Ge and GeSn NWs over conventional FET materials and architectures, as well as introducing the mechanisms of the growth and doping of semiconductor NWs and summarising the existing literature of doping of NWs, particularly focusing on *in situ* doping. Chapter 2 outlines the experimental methodology for the synthesis of the Au NPs used for NW synthesis, as well as the syntheses of Ge and GeSn NWs, as well as detailing the equipment and chemicals used. Chapter 3 details how the dopant molecules impact the morphology of the NWs, with decreases in the diameters and lengths of NWs in most samples. The dopants are also shown to decease the NW yield, with most samples yielding cubic crystalline NWs grown in the (111) direction. Dopant precursors are also shown to have prominent effects on the Sn concentration of GeSn NWs, as well as having more pronounced effects on the crystallinity of the NWs. These results are followed by conclusions and an outline of potential future work in this field.

Chapter 1

1.1 Germanium Nanowires

1.1.1 Motivation

The requirements of modern technology are quickly advancing beyond the capabilities of one of their key components; the conventional MOSFET. As predicted by Gordon Moore in 1965, [1] the amount of transistors needed per square inch of integrated circuits is doubling on a yearly basis, in turn meaning transistors must become smaller and smaller. Though classical designs of transistors have scaled down drastically in size, with channel lengths as low as 10 nm [2] and 7 nm [3,4] being produced in commercial devices, this is unlikely to continue. This rate of decrease in transistor size has been unable to keep up with the trajectory in Moore's Law, with Moore and others predicting devices not being able to meet requirements of technology after 2025, nor go below 7 nm in channel length.[5,6] At these sizes, the traditional architectures and materials for these essential components do not allow for adequate control of current, leading to leakage current, electrostatics and an unreasonable wastage of energy,[7] and thus, conventional MOSFETs are reaching the limits of their efficacy. The conventional methods of transistor fabrication are also reaching their limits. Therefore, there is an increasing need for novel device architectures and materials that perform more efficiently at sub 7 nm sizes in order to bypass the limits of classical device designs as predicted by Moore.

Si has traditionally been used as a gate material in transistors due to its stable oxide and high carrier concentration. Although Ge was used in the first transistor in 1947, [8] it fell out of favour due to its unstable oxides, difficulty in handling without surface

oxidation, and high cost compared to Si. Recently, however, Ge has been re-examined as a potential material in MOSFETs due to its higher carrier mobility and improved electrostatic control when compared to Si,[9] both of which potentially make it an ideal material for sub-7 nm FETs. A study by Claeys *et al.* compared Si and Ge as materials in field effect transistors (FETs). Though they found that Ge devices gave a much higher leakage current than Si at lower *p*-doping concentrations, when the dopant concentrations were increased, this difference in leakage current was vastly reduced. Ge also functioned at a much lower power than Si.[10] These initial results for channel widths of approximately 30 nm showed promise for further scaling down of Ge FETs, with further research successfully investigating sub-10 nm transistors using Ge.[11,12] Similarly, GeSn alloys provide the additional advantage of having a tuneable direct bandgap,[13] leading to a higher band-to-band tunnelling rate [14] which makes them ideal for use in the channels of newer FET designs, such as tFETs. Another important advantage of using Ge and GeSn as replacements for Si in transistor technology is their similarity to Si. Although a significant amount of research has explored different materials for use in FETs (Group III/V [15] and Group II/VI [16]), Ge and GeSn are Group IV materials. Thus, they can be processed using the fabrication facilities and processing techniques used for Si, as well as sharing many properties, such as their diamond cubic crystal structure. They will therefore be far easier to integrate into established manufacturing processes than other materials.

As well as research into new materials for electronics, there are a number of groups investigating novel FET architectures which allow better current control in the FET channel with minimum power wastage. These architectures include 3D structures, such as MuGFETs, with reduced short channel effects of drain-induced barrier

lowering, subthreshold slope degredation and saturation velocity and lower leakage currents compared to traditional FET designs.[17–20] Particularly promising are FETs which use NWs as the channel. Specifically, they have found uses as key components in JNTs [21–23] and tFETs.[24–26] The former of these shows potential for scaling below 10 nm due to its lack of junction avoiding the problems caused by the lack of control in short p-i-n junctions (junctions consisting of consecutive *p*-doped, intrinsic and *n*-doped regions), as well as its simplicity in design and homogeneous doping potentially leading to cheaper devices. The latter allows for lower-power devices due to the smaller amount of energy required to induce band-to-band tunnelling compared to using the standard field effect. Thus, NWs have an unquestionable potential to become a key component in state-of-the art transistor technology.

1.1.2 Initial Research

Wagner *et al.* [27] first reported the VLS growth of crystalline Si "whiskers" in the 1960's. While their study laid the foundations of NW research, these "whiskers" had diameters in the scale of microns.[28] It was not until 1998, when Morales and Lieber were successfully able to grow NWs at the scale of tens of nanometres that NWs became a viable option for use in nanoelectronics. Since then, much research has been carried out in the area of NW synthesis, with NWs being grown using a variety of different methods. These can be separated into two main categories; "top-down" fabrication and "bottom-up" growth.

The top-down fabrication of NWs involves etching away a material, *e.g.* a Si substrate, to form NW structures. Generally, NW structures are etched from wafers, followed by stress limited oxidation to coat the structures with an oxide, or trimming to further refine the structure.[29] Traditional fabrication methods use optical lithography,

specifically UV lithography, to pattern nanostructures. However, due to the requirements of state-of-the-art devices stretching beyond the scope of UV-lithography,[30] other lithographic techniques have been implemented for producing high densities of small diameter NWs, such as EBL,[31] IBL [32] and NIL.[33] These lithographic methods potentially give nanometer-level of control over NW architectures.[30] However, in spite of this, this lithographic methods have several limitations. For example, the composition of NWs produced are limited by the substrates from which they are etched. Additionally, the generation of precise, small diameter and high-density arrays of NWs can be very time consuming by lithography, and all of the material etched away from the substrate must be disposed of as waste, neither of which are ideal in large-scale manufacturing.

Bottom-up NW fabrication involves synthesising or "growing" NWs in a "self-assembly" type of process, usually in a gas or liquid phase. A popular bottom-up approach for growing NWs, particularly semiconductors, is via a VLS mechanism, as described in Figure 1.1. In the VLS mechanism, a precursor of a material of interest in the vapour phase, (*e.g.* diphenyl germane in the case of Ge), dissolves in a liquid phase seed, (*e.g.* Au), until the seed becomes supersaturated at which point crystalline solid layers precipitate from the seed in the form of a NW, (*e.g.* a Ge NW). The VLS mechanism was first observed by Wagner *et al.,* [27] who observed that when Au impurities were present on a substrate surface, the addition of SiH_4 gas at temperatures above the Au-Si eutectic temperature caused the growth of crystalline Si wire-like structures. They noted that globules of Au remained at the tips of the wires during their growth, and thus, it was deduced that these acted as sinks for Si atoms, as well as catalysts for the formation of the wires. The vast majority of Si NWs synthesised

have followed similar procedures to that reported by Wagner *et al.*, using SiH_4 as the gas phase Si precursor and Au as a prominent seed catalyst.[34–37] In their 1998 study, Morales and Leiber used laser ablation to generate Si NWs using a Si-Fe target as the "precursor". Since then, a variety of different precursors have been used to grow group IV and group III/V NWs [38–40] using of a variety of different seed catalysts, such as Al,[41] tin [42] and Bi.[43]

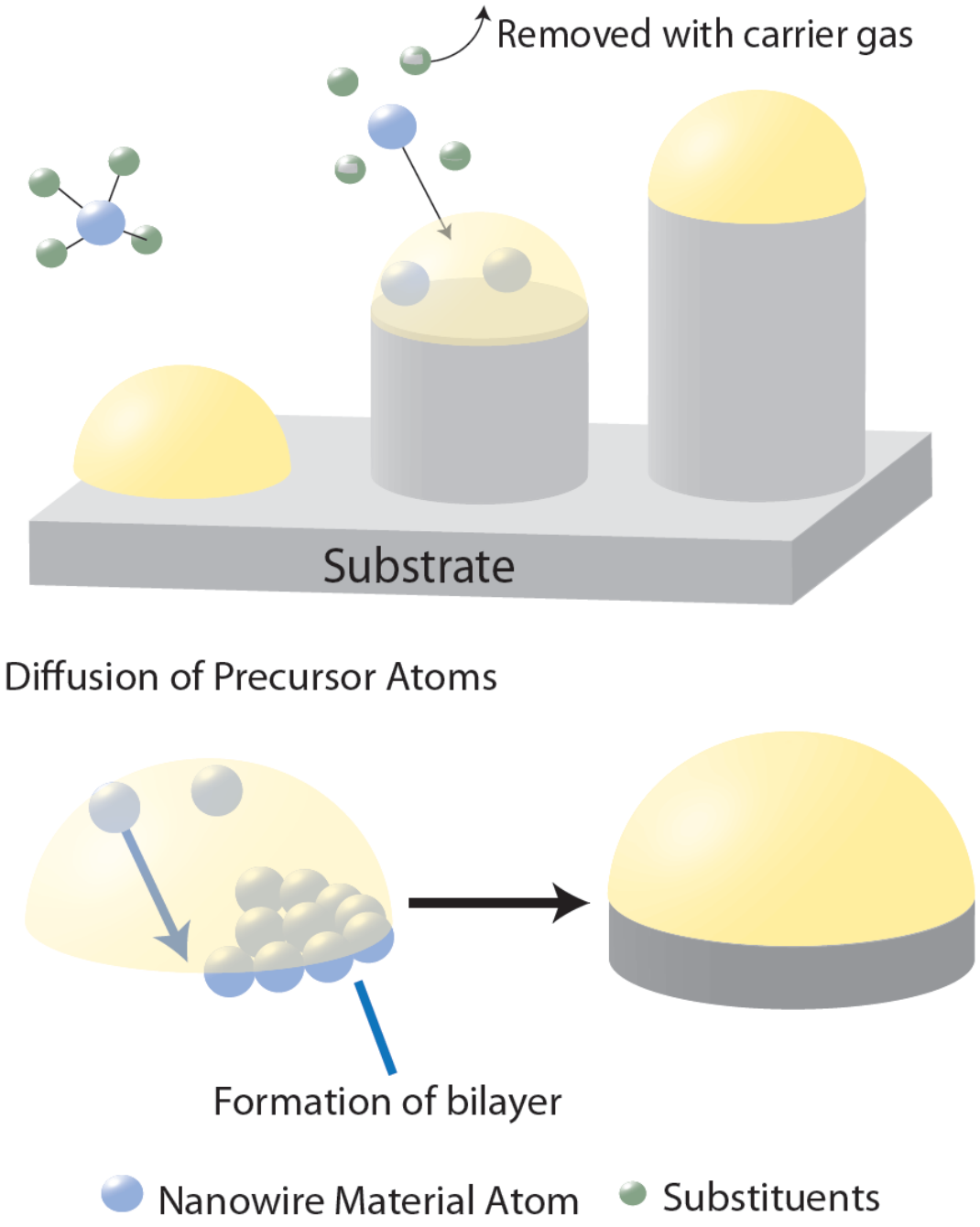

Figure 1.1: Schematic detailing the introduction of NW precursor molecules in VLS growth, the decomposition of molecules, the NW precursor atoms dissolving into the seed catalyst, and the formation of the bilayers that precipitates out to form the NWs.

Conventionally, the bottom-up growth of NWs is carried out using gas phase precursors, although several studies have used solid phase precursors in the form of powders. Sun *et al.* [44] reported the growth of Ge NWs from Ge powder where the powder was placed in an alumina crucible in a quartz tube and heated to a temperature

of 950 °C for 1 h, under a Ar flow of 50 sccm. The NWs formed had identical crystal structures and growth directions to those produced using gas phase precursors.[45] Additionally, Biswas *et al.* [46] have reported the use of liquid-based precursors for the VLS growth of GeSn NWs on Si substrates by CVD. Most solution-based synthetic approaches are, however, based around growing NWs from solution-based precursors and NPs, heated in an inert gas environment in a reaction flask,[47,48] *i.e.* via a solution-liquid-solid mechanism. Other examples in literature have demonstrated the successful growth of NWs from supercritical fluids, via a SFLS,[49,50] whereby precursors are introduced to seed catalysts suspended in supercritical fluids, such as carbon dioxide or hexane. Also reported are VSS methods,[41,51] and self-seeded NW growth.[52]

1.2 Doping of Nanowires

1.2.1 *Ex situ Doping*

One of the most essential steps in the process of manufacturing transistors is doping of the channel (NW), which involves the controlled addition of impurities into the crystal structure of a semiconductor to make either a *p*- and *n*- type material. Generally, transistors rely on altering the gate voltage to allow and block the movement of electrons. The efficacy at which this can be achieved is dependent on the number of free electrons or holes, which can be altered in a material by doping. In the case of group IV semiconductor materials, group III, (*e.g.* B, Al) and group V, (*e.g.* P, As), elements are used as *p*-type and *n*-type dopants, respectively. Boron (B) and phosphorous (P) are the most commonly used dopants in conventional group IV semiconductors, due to their high solubilities in Si and Ge. Traditionally, the doping of semiconductors is achieved by ion implantation which involves the bombardment

of a semiconductor material with ions of the dopant atom at high speeds. The bombardment is followed by a thermal anneal, whereby the material is heated to allow the dopant to diffuse throughout the semiconductor and promotes a uniform doping, as well as rectifying any crystal defects formed during ion bombardment. However, ion bombardment was designed to dope conventional thin film structures and accurately controlling dopant depth at small dimensions is difficult. Doping 3D device architectures, such as MuGFETs [53] or NW based FETs,[21] by ion implantation is also difficult as close neighbouring structures can often cause shadowing of the ion beam, resulting in non-uniform doping across the whole of the device, as shown in figure 1.2. As well as this, smaller architectures can be irreparably damaged by the bombardment, sometimes with the ions passing straight through the structures without doping them. Although capping layers of SiO_2 are often used to protect the crystal structures from the severe damage caused by ion bombardment, difficulties arise when applying this to bottom-up grown semiconductor NWs, thus, more efficient and less damaging doping methods must be employed for the doping of NWs.

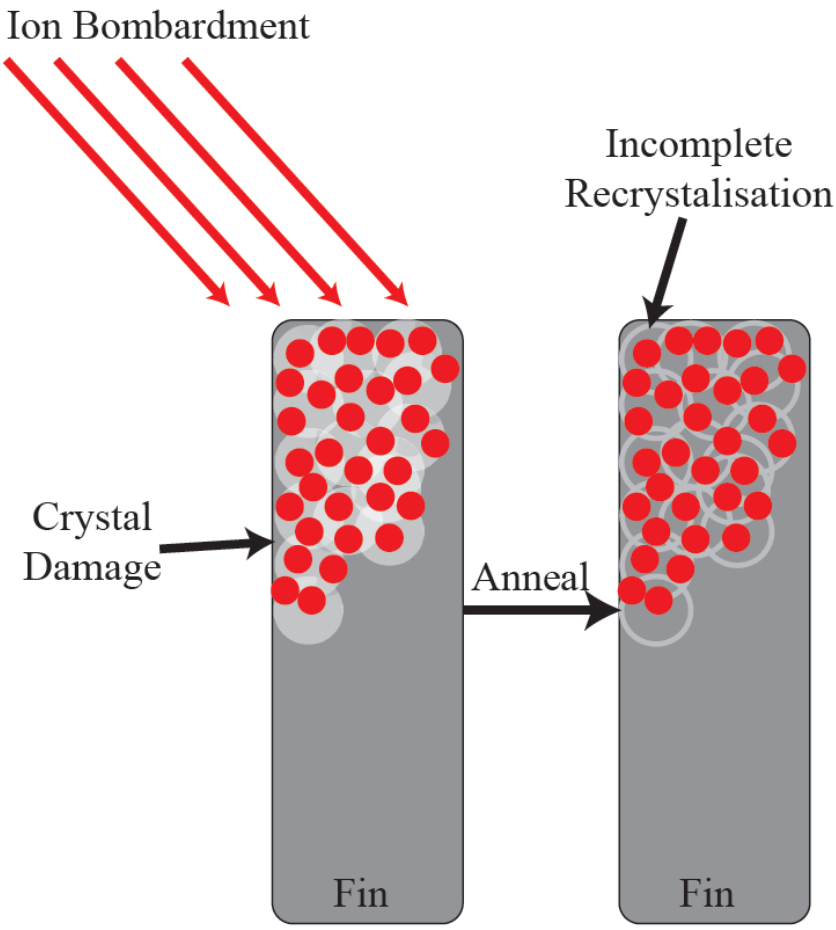

Figure 1.2: Schematic of potential damaging effects of ion implantations. Implant is unidirectional, leading to an inhomogeneous distribution of dopants, and subsequent incomplete recrystallisation during the anneal step.

Other *ex-situ* doping methods have been explored for doping semiconductors, the two most effective being MLD and SOD. MLD is a recently established process in the doping of bulk substrates, first reported by Ho *et al.* [34] who used the approach to dope Si wafers with B. MLD has since been used to dope a variety of semiconductor materials using a range of dopants.[54–59] MLD involves two steps: (i) functionalisation of a semiconductor surface with the dopant-containing molecule and (ii) its subsequent diffusion into the semiconductor via an annealing step. The functionalisation step is usually achieved by thermally-initiated hydrosilylation between the hydrogen-passivated surface of the semiconductor and a terminal alkene of the dopant molecule.

However, functionalisation using terminal alkyne groups,[32] as well as reacting hydroxyl-terminated surfaces with carbonyl-containing compounds [33] have also proven to be effective. Conventionally, rapid-thermal annealing is used to diffuse the dopant atoms into the semiconductor, usually with the use of a SiO_2 capping layer to prevent the diffusion of the atoms away from the surface.[57] SOD utilises a similar approach, although here, a solution containing the dopant is spin coated onto the sample requiring doping. The solutions used are most often composed of a dopant-SiO_2 mixture, or a polymer with Si and the dopant within its molecular structure. Rather than chemisorption, the dopant layers are attached to the surface of the substrates physically via an annealing step before diffusion.[60] While both of these methods allow for good control of dopant depth and are non-destructive, they both result in carbon deposition (and possibly contamination) on the surface of the doped substrate. Also, solutions used in MLD and SOD tend to be organic, leading to difficulties in obtaining an even coverage on the surfaces of small dimensional structures. A similar process to MLD was used by Hazut *et al.* to dope Si NWs using tetraethyl methylenediphosphonate and phenylboronic acid as P and B dopant molecules, respectively. This process was referred to as MLCD and involved the dopant molecules first being coated on a "donor" Si substrate, which was then placed on top of an array of NWs and annealed, resulting in doped NWs. This technique was used to achieve both homogenously P-doped Si NWs,[61] as well as doping parallel p-n junctions along Si NWs [62]. SOD has been used to dope Si NWs with B by Ingole *et al.*.[63] However, problems still arise when doping Ge and GeSn NWs specifically as annealing temperatures required for MLD, MLCD and SOD are often above 700 °C, which is greater than the melting point of small diameter Ge NWs and the segregation temperature for GeSn. Thus, other methods of doping must be employed.

1.2.2 *In Situ* Doping

The most prominently studied method for doping semiconductor NWs involves mixing and reacting dopant and semiconductor precursors together, typically in the gas phase, known as *in-situ* doping. *In-Situ* doping was first reported by Haraguchi *et al.* [64] for gallium arsenide (GaAs) NWs, but has since been extended to other NW systems, such as Si and Ge.[65–68] Typically, gas-phase *in-situ* doping of NWs takes place via a VLS mechanism, where both the NW and dopant atoms dissolve in the catalytic seeds and the dopant atoms form part of the crystal structure of the NW during nucleation.

Wallentin *et al.* [69] proposed a mechanism for axial dopant incorporation during *in-situ* doping of NWs, based on the Stringfellow model [70] of thin-film MOVPE. The mechanism Wallentin proposed, depicted in Figure 1.3 assumes the NW is growing at a steady state and outlines two competing growth mechanisms: axial growth caused by the nucleation of NW and dopant atoms through the seed catalyst and radial growth, caused by sidewall deposition, which can lead to tapering and facets along a NW. The model mainly focuses on axial growth, specifically the concentrations of the dopant in the solid, liquid and vapour phases (c_s, c_l, and c_v, respectively), along with the fluxes from the vapour to liquid (J^{LV}), liquid seed to crystal wire (J^{LS}) and the re-evaporation from the seed (J^{EV}). The flux of the seed metal itself into the crystal is also considered but is assumed to be negligible. Doping at the interface is assumed to occur in the same way as liquid-phase epitaxy, with segregation coefficients differing between dopants. Similar to the Stringfellow model, two types of dopant are identified. However, the Stringfellow model categorises dopants based on vapour pressure, the

Wallentin model examines dopant solubilities in the seed catalysts. Dopants of type A have low solubility in the metal seed, and high segregation coefficient in the solid NW, resulting in dopants being depleted out of the seed, and thus, a low $c_{l,}$ and a negligible J^{EV} so that $J^{LV} = J^{LS}$. Type A dopants include P in Si or Ge NWs using a Au catalyst, where the incorporation of P increases with increased molar fraction of the dopant precursor, until the point where solid solubility is reached.[71] Conversely, Type B dopants have a high solubility in the metal seed and a low segregation in the NW solid. Thus, J^{EV} is larger than J^{LS}, c_l is determined by the thermodynamic phase diagram of the vapour liquid system and the solid concentration is given by the segregation coefficient ($c_s = kc_l$). Antimony (Sb) acts as a Type B dopant in Ge NWs when using a Au seed catalyst, as was shown by Sutter and Sutter.[72] Their study used *in-situ* EDX measurements via TEM to show higher concentrations of Sb in the Au seed than in the NWs themselves.

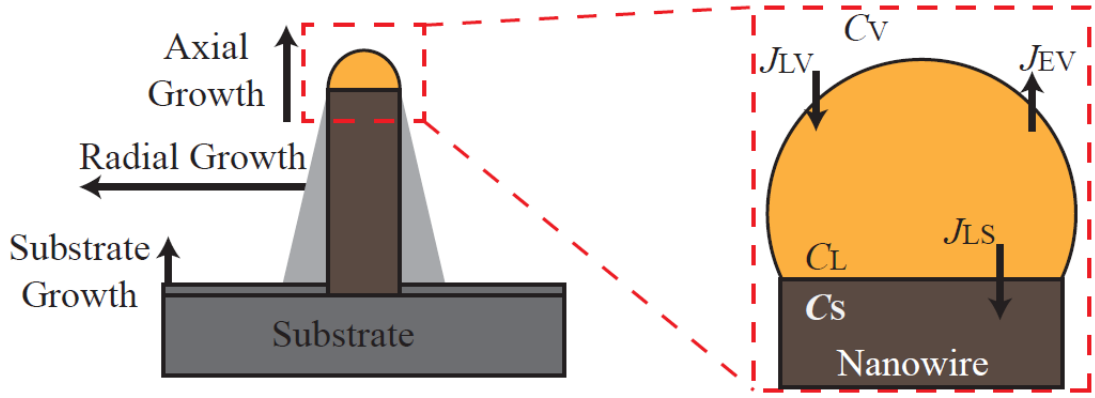

Figure 1.3: Schematic of dopant concentrations and fluxes during VLS growth, according to the Wallentin Model.[69] Left image shows directions of growth, highlighting how axial growth may occur through the seed, as well as growth on the substrate and radial growth occurring due to deposition of precursor atoms on substrate and NW surface, respectively. Right image shows the fluxes of dopants and their directions, and highlights the concentrations of the solid, liquid and vapour phases of NW growth.

One of the main disadvantages of *in-situ* doping is that the dopant molecules may not always be incorporated into the NW crystal structure. As outlined in the Wallentin model [69], along with the axial growth of NWs, dopants may also enter the NW from its side facets via an absorption-and-capture mechanism. Studies into both mechanisms have found that radial dopant incorporation is the more effective of the two,[73,74] resulting in NWs with non-uniform axial and radial doping profiles, with the majority of the dopant atoms being present on the sidewalls at the base of the NWs. This not only leads to a lack of control of the amount of dopant incorporated into the NWs, but has drastically adverse effects on the electrical properties of the wires, especially those which are designed for devices that require engineered axial doping profiles. As well as this, dopant precursors can severely affect the morphology of the NWs during growth. Some of the most prominent examples of this are seen in studies using B_2H_6 to dope Si [75,76] and Ge [77] NWs. Li *et al.*[75] observed faceting on the surface of Si NWs grown in the presence of B_2H_6. The lower dissociation energy of B_2H_6 compared to SiH_4 allows the former to react with incoming SiH_4, lowering its

decomposition temperature. This in turn leads to the growth rate of B-doped Si films increasing, which causes the faceting. Similarly, Lauhon *et al.*[76] observed the formation of amorphous Si-shells around the surface of Si NWs. This type of growth can lead to NWs tapering, which is unfavourable for a number of reasons. Firstly, during sidewall growth, Si atoms do not pass through the Au seed catalyst, instead forming polycrystalline Si, which increases the resistivity of the NW. Also, the non-uniform diameter formed when tapering occurs causes a variation in the properties along the length of the NW and the increase in sidewall deposition of dopants can impact the efficiency of a transistor. When synthesising NWs with axial *p-i-n* junctions, radial growth and doping results in radial *p-i-n* junctions, which parasitically impede performance. *In-situ* etching, both with HCl added to the reaction vessel,[78,79] and with the use of chlorine-containing NW material precursors that form HCl *in-situ* [80] have been successfully used to prevent tapering and thus, resolving non-uniformity caused by sidewall dopant deposition.[81] However, HCl is detrimental to most CVD apparatus, as etching of metals in the chamber and elsewhere causes contamination of samples and equipment damage. In cases where HCl is undesirable, tapering may also be prevented by lowering the temperature appropriately.[39] Outside of undesirable radial growth on NW surfaces, dopant precursors have been shown to inhibit NW growth, and in some cases completely prevent it. Schmid *et al.* [71] found that while PH_3 led to only a slight decrease in the growth rates of Si NWs at lower concentrations, at high enough concentrations, growth was completely inhibited. Similarly, AsH_3 has been shown to totally inhibit Si NW growth in relatively small concentrations [82] and trimethyl antimony has been shown to decrease the growth rate.[83] This has been attributed to a lowering of the surface tension of the Au melt by the dopant, thus preventing the dissolution and nucleation of NW atoms into the seeds,

though it is more likely due to the addition of P into the liquid seed, and altering the Au-Ge system.[71]

Altering the composition of the seed catalyst affects the chemical potential difference between adatoms of the NW growth material in both the vapour and solid crystal phases, known as supersaturation ($\Delta\mu$). This is due to the relationship between $\Delta\mu$ and the equilibrium concentration (C_e) for the bulk system, as outlined in equation (1).[84]

$$\Delta\mu = kT \ln \frac{C}{C_e} \quad (1)$$

where C is the concentration of the NW growth material, k is the Boltzmann constant, and T is the temperature.

This quantity is proportional to the growth velocity of the wire (v) as shown in equation (2).[84]

$$v \propto [(\Delta\mu)/(kT)]^2 \quad (2)$$

Thus, changes in the composition of the seed catalyst made by *in-situ* doping will directly affect the growth rate. In systems with only the seed and the NW material atoms, the equilibrium concentration will remain fixed, and thus, the growth velocity may be calculated at particular NW radii.[85] However, when introducing a dopant atom to the system, it becomes ternary, and thus, the fluxes of dopant and NW growth atoms entering the liquid-phase seeds will affect the equilibrium concentrations, and thus, will affect the chemical potentials, incorporation rates, and growth velocities of

NWs.[86] Therefore, calculating the effects that dopants will have on NW growth velocities are far from trivial, and dopant precursors will have even greater effects.

Conversely, several examples of *in-situ* doping of III/V materials have led to positive effects on NW morphology. Diethylzirconium has been shown to cause InP NWs to be grown with a purely zinc blend crystal structure, rather than the mixed crystal structure seen when undoped [87] and H_2S has been shown to induce a perfect wurtzite structure.[88] Dimethyl zirconium has also been shown to increase the growth rate of InP NWs.[89] The effects of dopant precursors on NW morphology have been circumnavigated to an extent through the use of non-Au seed catalysts. Examples in literature show that NW growth can be achieved using Bi,[90] Al,[91] and Ga [92] as seed catalysts, with the latter two incorporating atoms from the seed into the NWs to the extent that the NWs were doped. Although *in-situ* doping and its effects on Ge NW growth have been comprehensively studied, there are no examples in the literature to date of doping of NWs grown from solution, which was a focus of the research reported in this thesis. As well as this, there has been no published research on the doping of GeSn NWs by any methods.

In this vein, a significant advantage of *in-situ* doping is the large degree of control that can be obtained over dopant concentration, simply by altering the ratio of NW to dopant precursor used, as has been achieved in the gas phase.[93] Similarly, selectively opening and closing the flow of dopant precursor gases during growth allows for alternating intrinsic and doped regions in the same NW, or heterogeneous doping of NWs.[94,95] The latter is particularly useful, as heterogeneously doped NWs are needed for certain applications, *e.g.* NW tFETs [24] and *p-n* junctions for solar cell

applications.[94,96] Conventional doping methods are often unable to achieve the precision required to give the doping profiles necessary for these applications. Christensen *et al.* [97] achieved intrinsic regions of ~10 nm by *in situ* doping, highlighting the precision that can be achieved. As well as this, it is a far simpler doping method, being less destructive and requiring less processes involving heating and possible damage and alteration to the crystal structure than many *ex-situ* doping methods.

While *in-situ* doping using gas precursors has been widely studied, no research on the topic has been reported to date using liquid or solid NW or dopant precursors. Work has previously been carried out by Korgel *et al.* [98] and Biswas *et al.* [46] into the use of liquid-injection CVD to grow Ge and GeSn NWs, respectively, which paves the way for the use of liquid-injection *in-situ* doping. Liquid injection CVD can have the advantage over conventional gas-phase CVD in that it gives the potential for a greater control over morphology, as well as allowing for a continuous throughput process when scaling up towards mass-scale manufacturing.[99] However, as liquid-injection *in-situ* doping is a new field, new dopant precursors must be selected. For dopant precursors to be effective, a number of requirements must be met. Firstly, the dopant precursor must have a similar decomposition mechanism and temperature to that of the NW precursor. Secondly, both the dopant and NW precursors must be soluble in the same solvent. A final point to note is that the ratio of dopant to NW precursor in solution will rarely translate into the ratios within the NWs due to their differing solubilities in the metal catalyst. For example, both Ge and Sn have higher solubilities in Au than P at a growth temperature of 450 °C using liquid precursors. However, this has not proven to be problematic in conventional gas-phase CVD, and thus,

experiments shall be calibrated based on the ratios of P to Ge from the DPG and phosphine precursors, using similar or identical ratios to those previously used in literature.[79,93,100]

1.3 Characterisation Methods

Due to the reduced dimensions of NWs compared to bulk semiconductors, the characterisation of dopants in semiconductor NWs is far from straightforward. When doping bulk materials and wafers, Hall Effect measurements are generally used for characterisation, and while they may be used for NWs,[101] using this technique for NWs with diameters below the 100 nm range is extremely difficult. Additionally, EDX which is commonly used to measure the elemental composition of NWs has a margin of error of 0.5 at.%, which is too low to properly analyse the concentrations of dopant atoms required in NW samples.

Often, the most comprehensive method to characterise doping of NWs is electrically, either 2 or 4 probe contacts. The resistivity of NWs can then be qualitatively determined from equation (3):

$$\rho = \frac{\pi}{ln2} . \frac{V}{I} \qquad (3)$$

Here, V, I and ρ represent voltage, current, and resistivity, respectively. The resistivity of NWs can used to calculate active carrier concentration, using their relationship as shown in equation (4):

$$\mu_m = (q \times n_s \times \rho \frac{L}{A}) \quad (4)$$

where μ_m is the dominant carrier concentration, q is the elemental charge (1.602×10^{-19} C), n_s is the sheet density, and L and A represent the length and cross-section area of the section of the NW being measured, respectively.

Doping levels in semiconductor NWs can also be determined from NW-FET devices. NW-FETs are assembled by dropping NWs onto a substrate, usually an insulator, before placing metal electrical contacts onto each end of the wires. By sweeping the source-drain voltage and measuring the current, the NW conductivity can be determined which relates to carrier concentration as defined by equation (5):

$$\sigma = nq\mu \quad (5)$$

Here, n, q, and μ refer to carrier concentration, elemental charge and carrier mobility, respectively. Carrier mobility is in turn found by changing the potential of the backgate and measuring transconductance, which relate to each other as shown in equation (6):

$$g_m = \frac{C\mu}{L^2} V_{SD} \quad (6)$$

where g_m, C, L, and V_{SD} refer to capacitance, length of active region and source-drain voltage, respectively. While this method is effective, it can be difficult to fabricate effective NW-FETs for measurement. The doping concentration throughout a NW needs to be high to prevent depletion in the FET,[102] allowing it to act as a transistor,

and current to flow through. As well as this, the contacts to the NWs should be Ohmic rather than Schottky Barriers. Ohmic contacts are formed when there is a negligible resistance at the interface between a NW and the metal contact, whereas with a Schottky diode, the resistance at this interface is such that electrons must reach energy sufficient to jump from the conduction band of the metal to the conduction band of the semiconductor. Thus, if an Ohmic contact is not formed, the resistance of the contact is also measured electrically, and thus, must be distinguished from the NW resistance in order to use electrical measurements to analyse doping concentration. Also, any oxide layer present on the NW must be removed before contacting, which is difficult to achieve without causing damage, and high temperature recipes used for forming devices from bulk materials must be avoided, as these cause NWs to become metallic. Despite the difficulties, Ohmic contacts have successfully been created for both *p*- and *n*-doped Si [103,104] and Ge [65,105] NWs. One method of achieving this is by heavily doping both ends of the NW to ensure that they act electrically as metals, while leaving the centre of the wire lightly doped. [106,107] NW-FETs also allow capacitance-voltage measurement, which give information on carrier density by measuring capacitance as a function of the gate voltage. By careful screening, it is possible to use this method to find carrier mobilities [108] and surface state energies,[109] and is capable of analysing the resistivity of NWs when coupled with conductive AFM.[110] Though effective, the cost and time required to manufacture NW-FETs is excessive for quantitatively analysing the levels of doping within the NWs.

Optical measurements may also be used to characterise doping, often being advantageous in requiring no sample processing beforehand. Raman spectroscopy has been used in several cases to quantitatively measure doping. Kawashima *et al.* [111]

observed a broadened signal at high wavenumbers in highly B-doped Si due to intra valence band hole excitation, and following this, Fukata *et al.* [93] studied whether Raman spectroscopy could be used to quantify doping in Ge NWs. They observed an asymetric broadening of the 300 cm^{-1} Ge-Ge peak, which increased with increasing dopant concentration. This increase was attributed to the electrically active electrons in the NWs, due to Fano interference from discrete optical phonons coupling with electrons in the continuum inter-band due to the increased presence of holes or electrons.[93] This interference changes as a function of energy, and thus, asymmetric peaks are observed in the Raman spectra, known as Fano Broadening.[112] They also observed two peaks of Ge-B, and a Ge-P peak at 544 cm^{-1}, 565 cm^{-1} and 442 cm^{-1}, respectively. These peaks also increased in intensity with an increase in B_2H_6 and PH_3 flows, as well as correlating with the shift calculated from previous results in the experimental doping of Si NWs. With the use of the Fano equation[113,114] to quantify the broadening, approximate quantitative measuring for doping in the NWs was also achieved.

ESR has also been used to analyse P and B doping in Si NWs.[115,116] This simple technique, whereby properties of the electrons of a sample are analysed using a static magnetic field and microwaves, gives information on the interactions between electrons and nuclei. The values of orbit levels occupied by electrons will differ for the dopant and the semiconductor and thus, doping may be qualitatively analysed using this technique.

One of the most comprehensive methods of dopant characterisation is APT, whereby a sample is bombarded with x-rays, and atoms ionised, and directed towards a time-

of-flight detector. This method not only allows dopant concentration to be measured, but also allows for atom-by-atom 3D models of NWs to be constructed.[117] However, while immensely powerful, APT has drawbacks in that is requires lengthy sample preparation, is only able to analyse around 200 nm segments of NWs,[118] and is unable to measure active carrier concentrations.

Chapter 2

2.1 Nanostructure Synthesis

All chemicals were purchased from Sigma Aldrich, with the exception of DPG, which was purchased from Fluorochem.

2.1.1 Nanoparticle Synthesis

Dodecanethiol (40 μL) stabilised Au NPs were synthesised in a chloroform solution using a reduction of chloroauric acid (0.118 g), using tetraoctylammonium bromide (1.0936 g) as the phase transfer catalyst and sodium borohydride (0.1663 g) as the reducing agent following a procedure used by He *et al.* to synthesise Au-Ag NPs.[119] Once synthesised, the NPs were washed three times in ethanol, and added to 10 mL of toluene.

2.1.2 CVD Nanowire Synthesis

NWs were synthesised using a solution-based CVD technique. Si (001) wafers were sonicated for 10 min in acetone and 10 min in IPA and spin-coated with Au NPs at 2000 rpm for 30 s twice. The Au coated wafer was placed into a stainless steel HiP MS-11-AF1 microreactor connected with metal tubing and left under vacuum heated to 180 °C in a tube furnace overnight to remove any traces of water from the apparatus. The Si substrate was annealed in the microreactor for 1 h at 440 °C under a H_2/Ar atmosphere. Precursor solutions in toluene were prepared in a N_2 glovebox; DPG was used as the Ge precursor. DPG concentrations in toluene solutions were kept at 13 mM. For the syntheses of GeSn NWs, ATBS was used as the Sn precursor at a concentration of 2.4 mM in the toluene solutions. DPP, ADPP and TOP were used as

P precursors. These were varied in their concentrations from 44 μM to 278 μM in order to achieve atomic P/Ge ratios of 2, 1 and 0.2 % (2.7, 1.5 and 0.5 % for DPP, due to the difficulties making solutions with lower P/Ge atomic ratios). The precursor solution was loaded into a Hamilton sample lock syringe within the N_2 glovebox. Injection took place at 1.5 mL h^{-1} for 2 h with a H_2/Ar flow at 0.6 mL min^{-1} throughout the growth. The reactor cell was allowed to cool to room temperature before disassembly to remove the growth substrate.

2.2 Characterisation

2.2.1 Microscopy

All NW samples were imaged using an FEI Helios NanoLab 600i scanning electron microscope (SEM) at 5, 15, 20 and 30 kV. EDX measurements were taken and recorded in high-angle annular dark-field mode in a FEI Helios Nanolab 600i operating at 30 kV and 0.68 μA. TEM images were acquired using a Joel JEM-2100 operating at 200 kV in bright-field conditioning for imaging. For SEM analysis, the growth substrates covered with NWs were fastened onto SEM stubs using carbon tape. For scanning TEM (STEM) and TEM analysis, samples were dropped onto lacy-carbon copper TEM grids. NWs were removed from the substrate by sonicating a small segment of the sample in 0.25 mL IPA for 1 min, before dropping onto a grid and drying for 2 h. Percentage coverage was measured from the SEM images using a program coded in Java in-house, in which images were polarized by converting each pixel of the greyscale image above a certain level of brightness was converted to white, and each pixel below that level was converted to black, forming a binary image. The program then calculated the percentage of image that was white in order to provide an

estimated percentage coverage on the substrate. A brightness level of 288 was selected for Ge NWs, and 420 was selected for GeSn NWs.

2.2.2 Spectroscopy and Diffraction Measurements

Raman measurements were carried out using a Renishaw inVia Raman Spectrometer equipped with a 2400 lines/mm grating and a 514 nm laser. Spectra were collected with the use of a RenCam CCD camera, with beams focused on samples under a 50 × objective lens and measurements taken using a laser power of 1.9 mW. Measurements were made of single NWs. Samples were prepared for analysis by sonication as with STEM and TEM samples, dropped onto Si wafers, and left to dry for 2 h. XRD measurements were taken using a Philips X'pert Pro MPD equipped with a Panalytical Empyrean Cu x-ray tube and a Philips X'celerator detector.

2.2.3 Electrical Measurements

Undoped and doped Ge NWs were sonicated from the growth substrates in IPA and drop-cast onto 300 nm SiO_2/Si substrates. Contacting of individual NWs was carried out using UV and electron-beam (e-beam) lithography. Native oxides were removed from the NW surfaces before the deposition of electrodes using a 2 min dip in deionised water. Electrical tests were also carried out after using HBr and citric acid as oxide removal agents. Ti/Au and Pd were both used as electrode materials.

Doped GeSn NWs were electrically tested using a pre-patterned SOI substrate with an oxide layer of 90 nm, previously cleaned by dipping in acetone for 3 min and IPA for 2 min. NWs were mechanically transferred by brushing first the growth substrate and then the SOI substrate using a cleanroom tissue to ensure homogenous distribution of the NWs. After transfer, a Raith e-beam lithography system was used to create

contacts onto the NWs using a PMMA resist. After exposure, the patterned substrate underwent metal evaporation to deposit 40 nm of Ni and 80 nm of Au, with a subsequent lift-off process.

Chapter 3

3.1 *In situ* Doping of CVD Grown Ge NWs

3.1.1 Microscopy of *in situ* Doped Ge NWs

SEM and TEM were used to analyse the morphology and crystal structure of the doped Ge NWs synthesised. Figure 3.1(a) shows an SEM image of undoped Ge NWs grown on a Si substrate. These NWs could be produced in high yields, giving approximately 92.3 % coverage of the substrate, as shown in Table 3.1, and they displayed a straight morphology, with a slight curvature for the longer NWs. In comparison, SEM images of doped Ge NWs showed that the dopant precursors affected NW morphology and yield. ADPP and DPP had the most pronounced effects. Ge particles were observed in samples grown in the presence of 2 and 1 at. % P/Ge ADPP, (Figures 3.1(f) and (g), respectively) and an organic film was observed across the NWs in samples grown in the presence of 2.7 and 1.5 at. % DPP (Figures 3.1(b) and (c), respectively). More notable, however, was the decreased yield and length of the NWs in all four samples when compared to undoped Ge NW samples. As shown in Table 3.1, substrate coverage of Ge NWs was below 50 % for all of the samples doped with phenylated phosphines; with ADPP doped Ge NWs giving coverages of less than 30 % at all P/Ge ratios. The mean length of NWs doped with phenylated phosphines was around 70 μm, compared to those of undoped Ge NWs with mean lengths of approximately 200 μm. There was no observed faceting nor tapering of the NW sidewalls in the doped samples, which implies that neither DPP nor ADPP caused a decrease in the decomposition temperature of DPG; as was observed with gas phase *in-situ* doping of Si NWs with B_2H_6.[75,76] However, the presence of organic films and Ge NPs indicates

that interactions between DPG and the phenylated phosphines does occur to some degree.

Table 3.1: Approximate percentage coverages of Ge NWs on substrates taken from 12 μm^2 SEM images of NWs

Dopant Precursor	P/Ge at. %[1]	Percentage Coverage
Undoped	-	92.3
DPP	2.7	6.2
DPP	1.5	48.1
DPP	0.5	28.6
ADPP	2	19.7
ADPP	1	4.3
ADPP	0.2	19.5
TOP	2	46.2
TOP	1	88.0
TOP	0.2	49.0

1. Values calculated by measuring the percentage of SEM image composed of NWs via a Java program written in-house that calculated the percentage of the image above a certain brightness in order to give an estimate of wire coverage.

Conversely, SEM images indicated that TOP has little effect on the yield and lengths of the NWs produced (Figures 3.1(h)-(j)). The mean length of TOP doped NWs were approximately 150 μm, with substrate coverages above 45 %, as shown in Table 3.1.

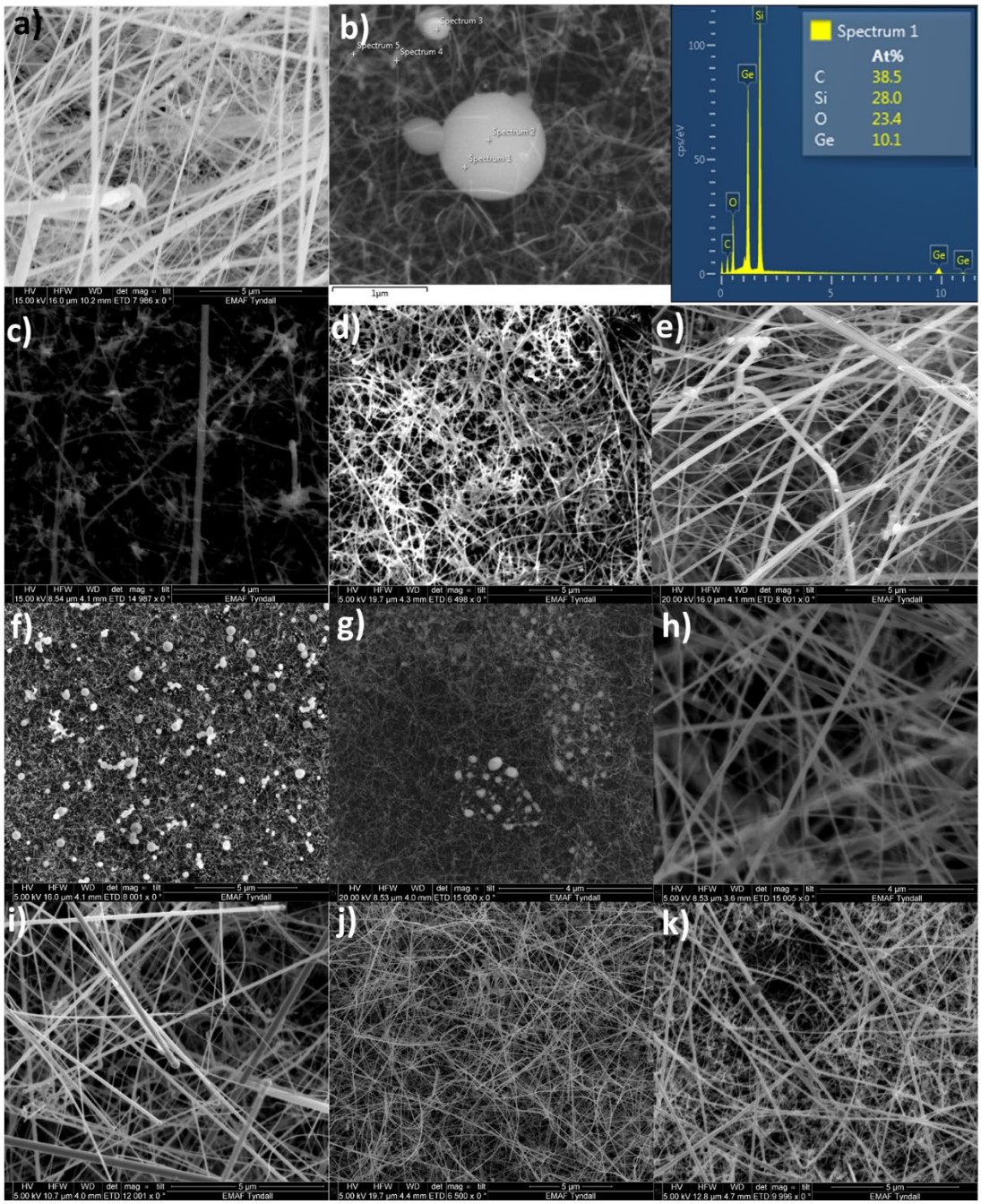

Figure 3.1: SEM images of Ge NWs grown from DPG and various P dopants under the following conditions: (a) an undoped sample, (b) SEM image and point EDX spectra of Ge particle on growth substrate surface from sample shown in (c), (c) DPP at 2.7 at. % P/Ge, (d) DPP at 1.5 at. % P/Ge, (e) DPP at 0.2 at. % P/Ge, (f) ADPP at 2 at. % P/Ge, (g) ADPP at 1 at. % P/Ge, (h) ADPP at 0.2 at. % P/Ge; (i) TOP at 2 at. % P/Ge, (j) TOP at 1 at. % P/Ge and (k) TOP at 0.2 at. % P/Ge.

TEM images of the doped and undoped Ge NW samples showed that crystalline NWs were obtained under all experimental conditions, and all NWs possessed a GeO_2 surface coating (Figure 3.2). Although most of the undoped and doped Ge NWs

produced were straight, some of the NWs in both the undoped and doped samples were kinked. NWs of diameters between 30 and 50 nm were used to measure the lattice spacing in order to determine the growth direction. All samples yielded NWs in the growth direction of (111) at these diameters (Figure 3.2) which is consistent with literature examples of Ge NWs of similar diameters grown via CVD.[120]

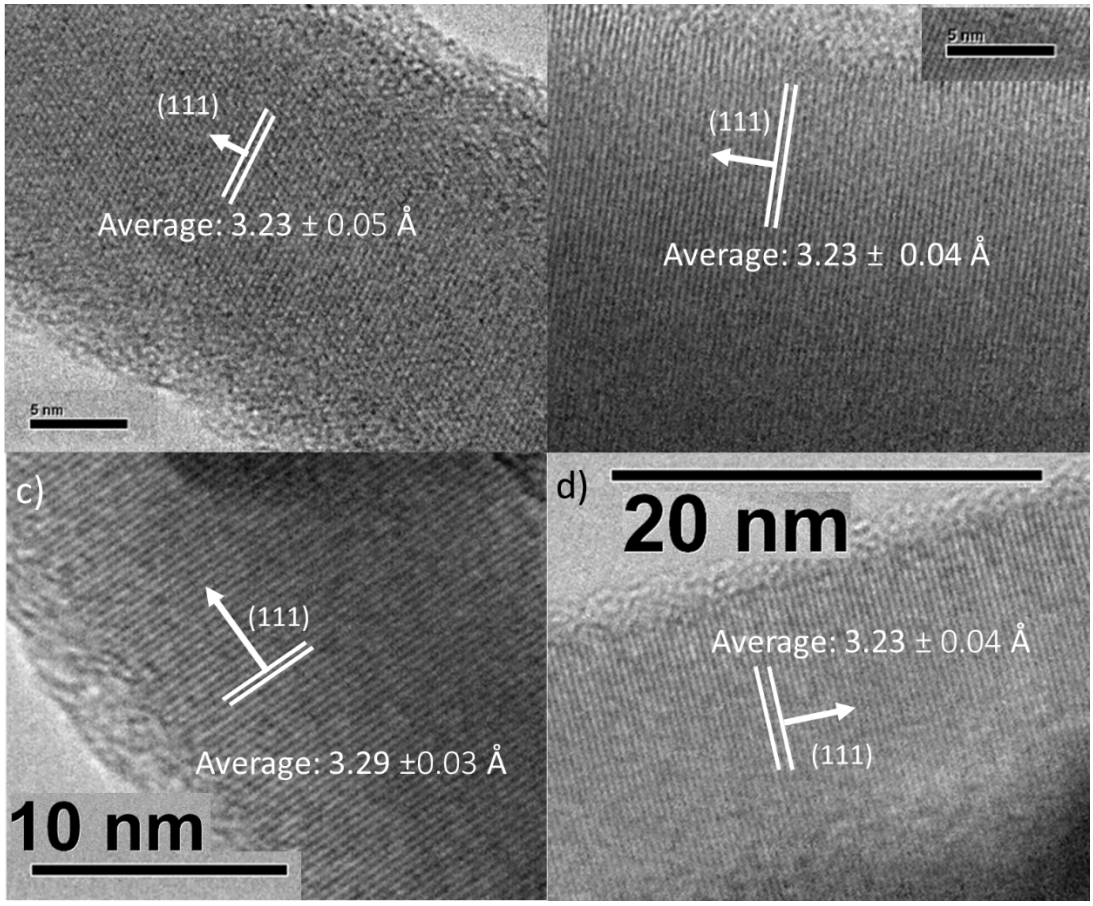

Figure 3.2: TEM images of (a) an undoped Ge NWs grown and Ge NWs grown in the presence of three different doping precursors: (b) 2.7 at. % DPP, (c) 2 at. % P/Ge ADPP and (d) 1 at. % TOP.

TEM images were also used to analyse diameter distributions across the samples, as well as distinguishing the crystalline cores of the NWs from their amorphous oxide shells. As seen in Figure 3.3, all three dopant precursors caused a notable decrease in the mean diameter of the Ge NWs compared to undoped NWs. As expected, NWs grown at the lowest dopant concentrations of 0.5 at. % for DPP and 0.2 at. % for ADPP and TOP, had a minimum effect on the mean diameter of the NWs compared to

undoped samples, *i.e.* 35, 30 and 50 nm for DPP, ADPP and TOP respectively compared to 60 nm for undoped. NWs grown in the presence of medium dopant concentrations, *i.e.* those with around a 1 at. % P/Ge ratio, had the lowest mean diameters, with values at least 10 nm lower than the other two concentrations of each precursor. This was most notable when ADPP was used as a dopant precursor. These drops in mean diameter, length and yield when compared to undoped NWs are likely a result of the effects of P on the kinetics of the Au-Ge system. P has previously been shown to lower the growth rate of Si NWs, [82] though the cause of this has never been directly studied. The same has been observed for Ge NWs grown using gaseous precursors.[86] In Si, this has been attributed to the lowering of the Au surface tension by P,[82] though it is more likely due to the effects of P on the equilibrium concentrations in the Au seed. This is most plausibly due to an increase in the chemical equilibrium concentration, possibly as a result of the flux of P into the Au seed, which would lower the chemical potential and the incorporation rate of Ge atoms into the Au seed, thus, lowering the growth rate. The difference seen in Ge NWs doped using phenylated phosphines may be due to interactions with DPG, preventing it from entering the Au seeds, and thus, slowing and inhibiting growth to a further extent. Interestingly, the slight drop in diameter distributions of 1.5 at. % P/Ge DPP and 1 at. % P/Ge TOP and ADPP samples meets with a slight decrease in the mean diameter for these wires when compared with their counterparts at other at. % of P/Ge. This is potentially due to the effects of P on the Au surface tension, though more work would need to be carried out to establish to what extent this occurs.

While the tight distribution of small diameters of the 1 at. % ADPP NWs may seem promising for narrow-channel NW-FET applications, these wires were highly

unstable, and were greatly affected by TEM and SEM analysis, as well as having the lowest percentage coverage. This, and the generally low yields of ADPP doped NWs highlights the unreliability of ADPP as a dopant precursor. Most notable across all diameter distributions was the lesser effect that TOP had on percentage coverage, NW lengths and NW diameters compared to the two phenylated phosphines. Therefore for this system, TOP was the best precursor for growing high yield of doped, straight NWs.

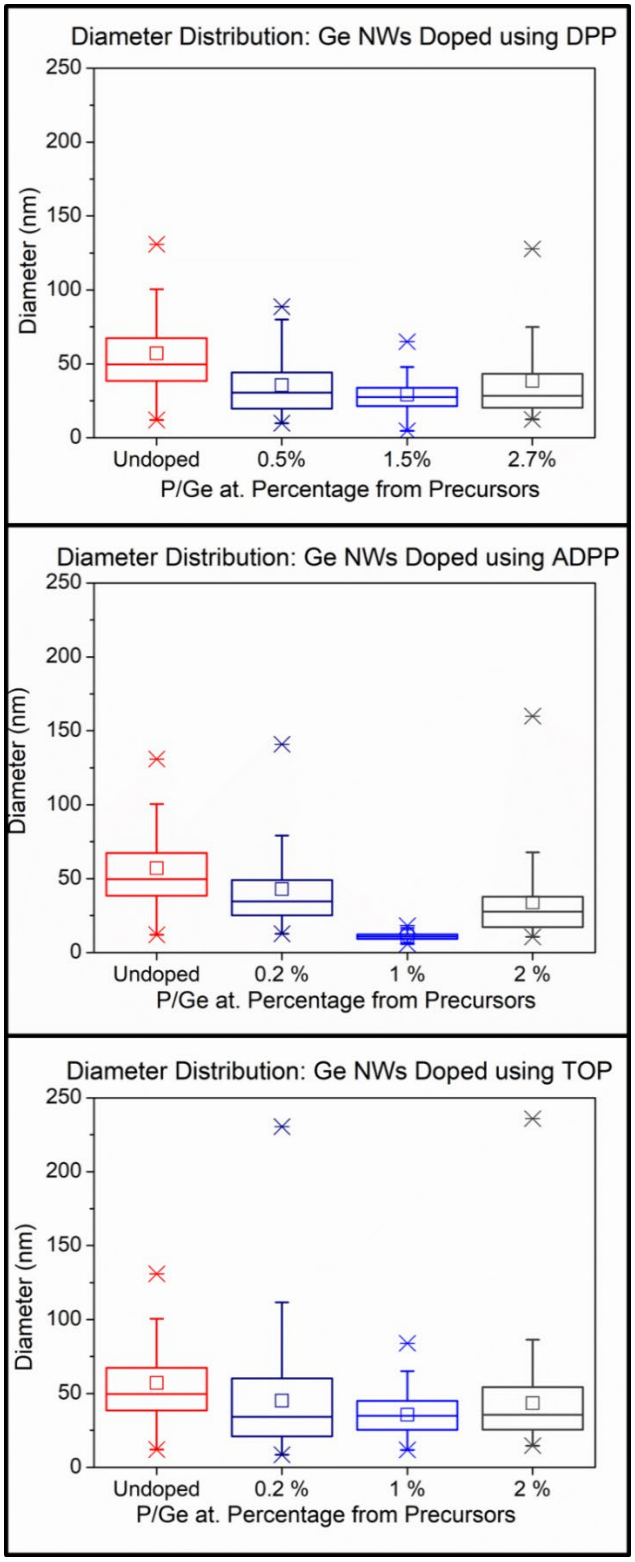

Figure 3.3: Box plots showing diameter distributions of Ge NWs in the presence of different concentrations of each dopant precursor. The crosses represent the maximum and minimum values, the small boxes represent the mean value, the larger boxes represent the 2nd and 3rd quartiles, and the lines extending from the large boxes represent the 1st and 4th quartiles.

TEM was also used to measure the thickness of the shells around the NWs, in order to determine whether they were composed of oxides or amorphous Ge deposited on NW sidewalls. Many dopant precursors in gas-phase *in-situ* doping have been shown to promote radial growth in both Si and Ge NWs.[75,77,121] As the *in-situ* doped NWs have shells with a smaller mean thickness than the undoped NWs, it appears that no radial growth is promoted by any dopant precursor. The larger shells for the undoped NWs are likely due to exposure to ambient air for longer than the previous samples leading to the formation of thicker oxide shells, as initial analysis of the NWs carried out after less time in air generally gave shell thicknesses below 5 nm. Although all samples were stored under ambient air, some samples of NWs were exposed for longer than others Typically, NWs were exposed to ambient air for approximately 1 month. TOP and DPP yielded oxide shells with a similar mean thickness to the undoped samples, with a mean shell thickness of 8 nm. NWs were etched in HF, and the removal of this outer shell ensured that these layers were in fact composed of GeO_x. Potentially, the P from the dopant precursors may become incorporated into the wire via the sidewalls, as has been reported in literature [122] and this may decrease the oxidation rate of the Ge surface of the NWs. As the sidewalls of the NWs grown in the presence of TOP had oxide shells of a similar thickness to undoped wires, the indication here is that P atoms are incorporated into the NWs via the sidewalls to a lesser extent in TOP and DPP than for ADPP grown NWs due to the thinner oxide layers seen in the latter samples.

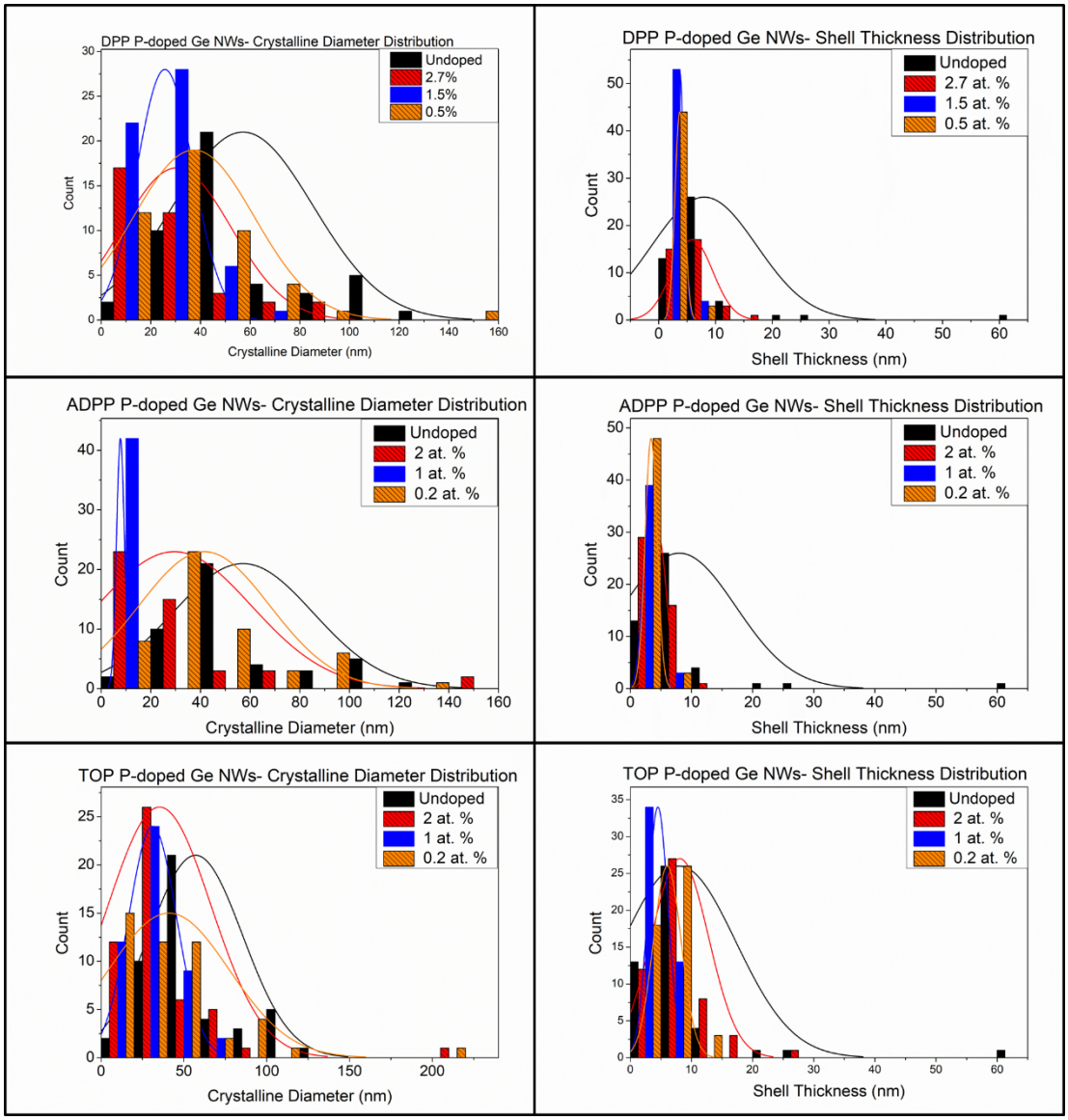

Figure 3.4: Diameter distributions of crystalline NWs and their corresponding oxide shell thickness for undoped and doped Ge NWs.

3.1.2 Spectroscopy of *in-situ* Doped Ge NWs

Raman data for all samples (Figure 3.5) showed clear evidence of a Ge-Ge transversal optical phonon mode peak at approximately 300 cm^{-1}, indicating that all of the NWs synthesised had cubic crystal structures, in agreement with the TEM results.

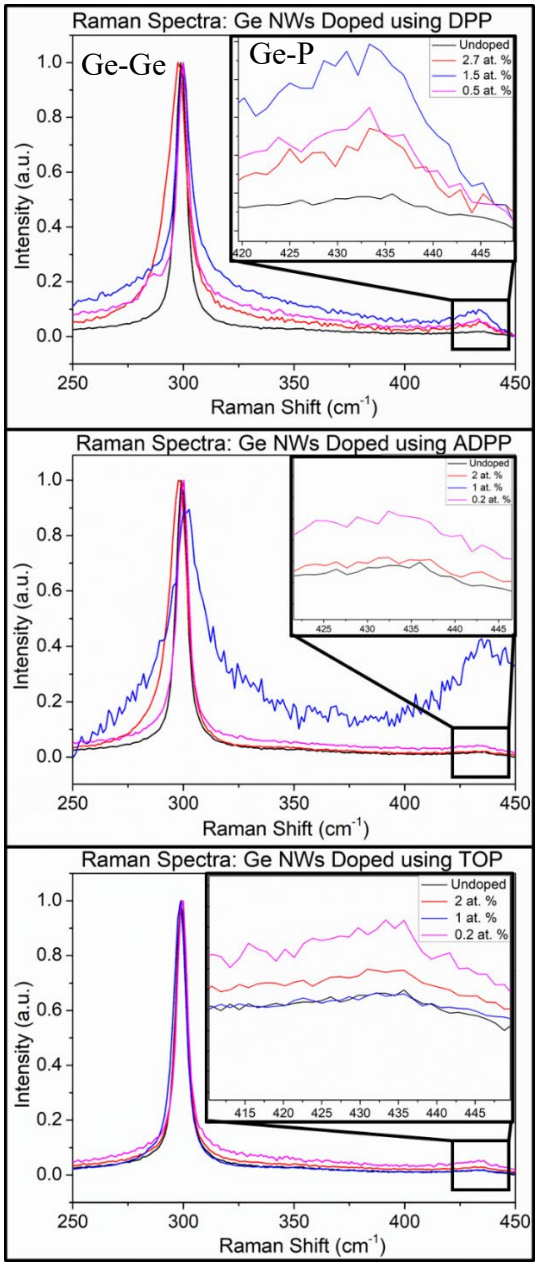

Figure 3.5: Raman Spectra for Ge NWs grown in the presence of differing concentrations of each dopant precursor. DPP reactions carried out with 2.7, 1.5 and 0.2 at. % P/Ge; ADPP and TOP reactions at 2, 1 and 0.2 at. % P/Ge.

Quantum confinement effects, due to the nanometre-scale diameters of the NWs, resulted in a red-shift of the Ge-Ge transversal optical phonon mode peak for both doped and undoped NWs to lower wavenumbers compared to the value of 300 cm^{-1} obtained for bulk Ge. The large signal-to-noise ratio in some of the Raman spectra, particularly prominent in the 1 at. % P/Ge ADPP sample, was likely due to the laser

beam interacting with the Si substrate, or particles deposited from the IPA solution, as opposed to smaller diameter NWs. Ideally, NWs with identical diameters would have been used for each measurement. However, this was not feasible with the Raman spectrometer used, which had a microscope with a maximum magnification of ×50, making it impossible to measure NW diameters with any accuracy. A peak at approximately 435 cm^{-1} was observed for most of the doped NW samples analysed but was not observed in undoped NW samples, which may be attributed to the presence of Ge-P bonds.[93,100] All of the doped NW samples showed a red-shift of this peak towards lower wavenumbers compared to Ge-P peaks reported in the literature.[93,100] Red-shifts in the Ge-P peak were seen by Futaka *et al.* [93] when lowering the flow rate of PH_3 in their gas based *in-situ* doping, thus, lowering the P concentration in the NWs. Therefore, the lower wavenumber peak observed here compared to the results in previous work may be due to a lower concentration of P in the NWs presented here. This Ge-P peak is least prominent for samples grown with ADPP. Though the Ge-P peak from the 1 at. % P/Ge sample is intense in the spectrum shown in Figure 3.5, this is unreliable, as this spectrum had the lowest intensity before normalisation, as shown in Figure 3.6(a). Fano broadening similar to that seen by Fukata *et al.* [93] was also observed in each spectrum, which is to be expected from the addition of P due to the increased presence of electrons compared to the Ge NWs, which may couple with discrete photons to cause Fano interference. Though promising, this cannot be comprehensively attributed to electrically active P present in the NWs. The extent of Fano broadening not only varies in each sample in a way that does not match with trends in concentration; it also varies between different NWs from the same sample (example given in Figure 3.6(b). This is likely due to the different diameters of each sample, which would have significant effects on the peak widths. In spite of this, the

trends of DPP an ADPP samples give reasonably good correlation between Fano broadening and dopant concentration, when accounting for the noise in peaks.

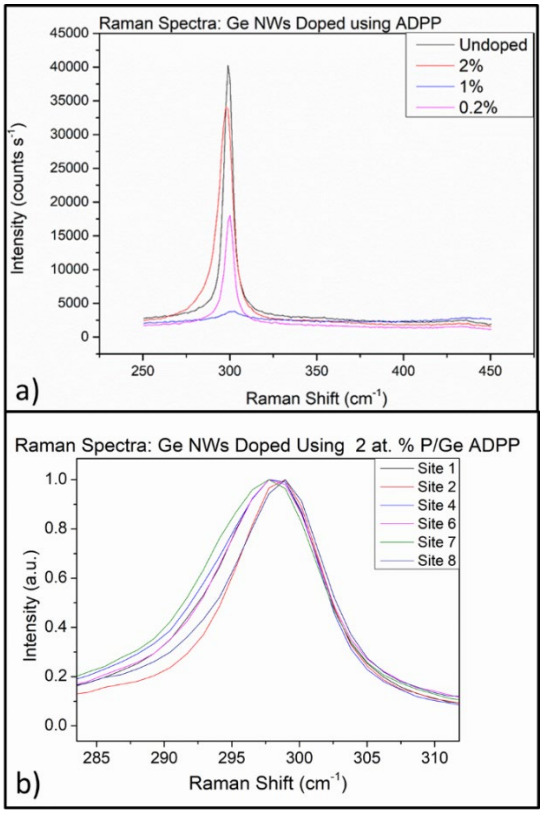

Figure 3.6: (a) Raman spectrum of Ge NWs grown in the presence of differing concentrations of ADPP before data was normalised; (b) Raman spectrum of different wires from 2.7 at. % DPP doped sample of Ge NWs showing variation of the Ge 300 cm^{-1} peak and Fano Broadening.

All of the doped and undoped Ge NW samples had cubic crystal structures based on XRD analysis, as shown in Figure 3.7, which matched well with TEM and Raman data. All but one of the samples showed diffraction peaks corresponding to (111), (220) and (311) diffraction planes. Only the undoped Ge NWs, and samples grown in the presence of the lowest concentrations of dopant precursors, showed (400) and (331) diffraction peaks, probably due to the higher yield of these samples on the growth substrates. The broad peaks at around 69° (2θ) can be attributed to the (400)

diffraction peak from the Si substrate. A diffraction peak was observed for Ge NWs grown in the presence of the 0.2 at. % TOP dopant precursor at 28.5° (2θ), which is close to the (102) diffraction plane for tetragonal Ge (27°). Also, Ge NWs grown in the presence of 1.5 at. % and 0.5 at. % DPP both displayed a diffraction peak at approximately 33° (2θ), which matches with the (212) diffraction plane for tetragonal Ge. However, as neither the Raman nor the TEM data obtained showed any evidence for tetragonal Ge NWs, these peaks are likely to be unrelated to the Ge NWs, and may instead be attributed to the Si substrate.

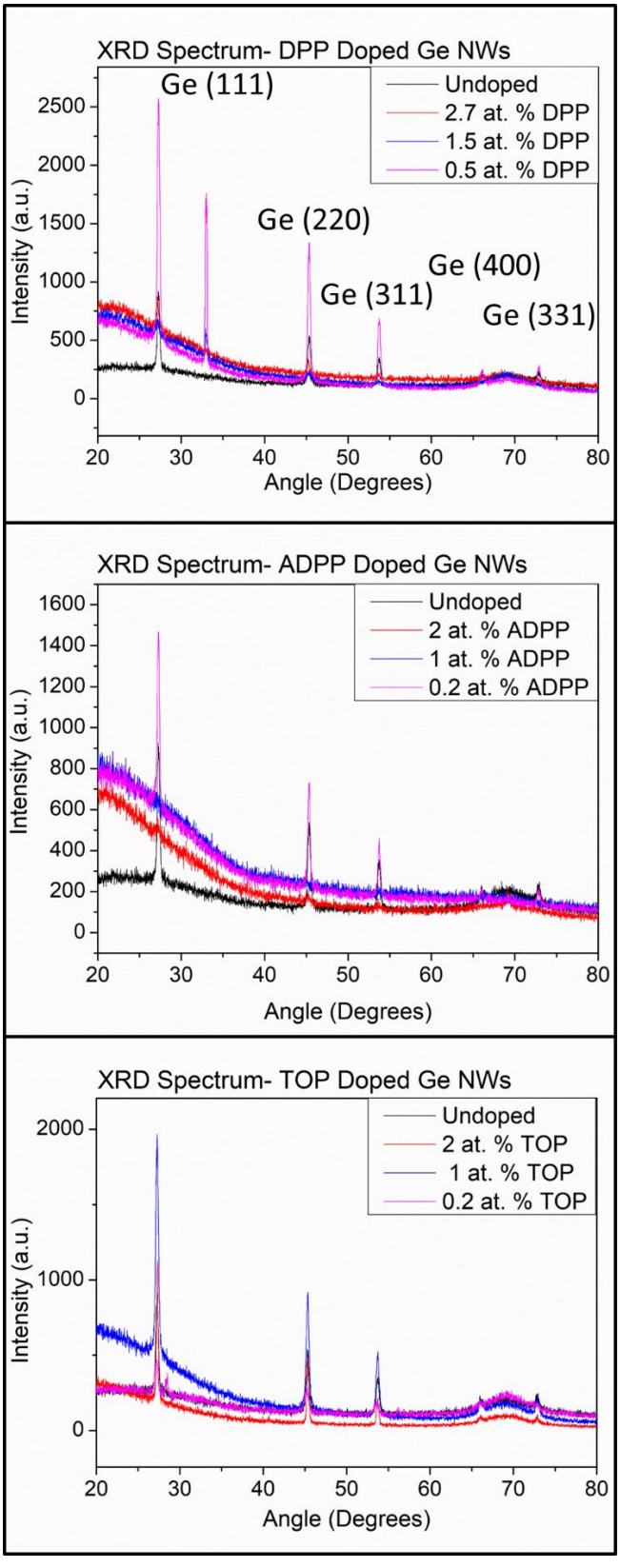

Figure 3.7: XRD diffraction patterns of undoped and doped Ge NWs grown using different P dopant precursors at differing concentrations. Peaks labelled in DPP diffraction pattern according to research by Korgel *et al.*[48]

3.1.3 Electrical Testing of *in-situ* Doped Ge NWs

All of the doped Ge NWs synthesised in this project were found to be insulating under an applied electric field of up to 500 V μm^{-1} and a voltage in excess of 50 V (applied between source and drain electrodes). This insulating behaviour remained even when the NWs were exposed to deionised water, HBr and citric acid treatments to remove the surface oxide before deposition of metal contacts. Additionally, the undoped Ge NWs synthesised in this project were not found to be conducting. NWs remained intact throughout the measurements, as shown in Figure 3.8.

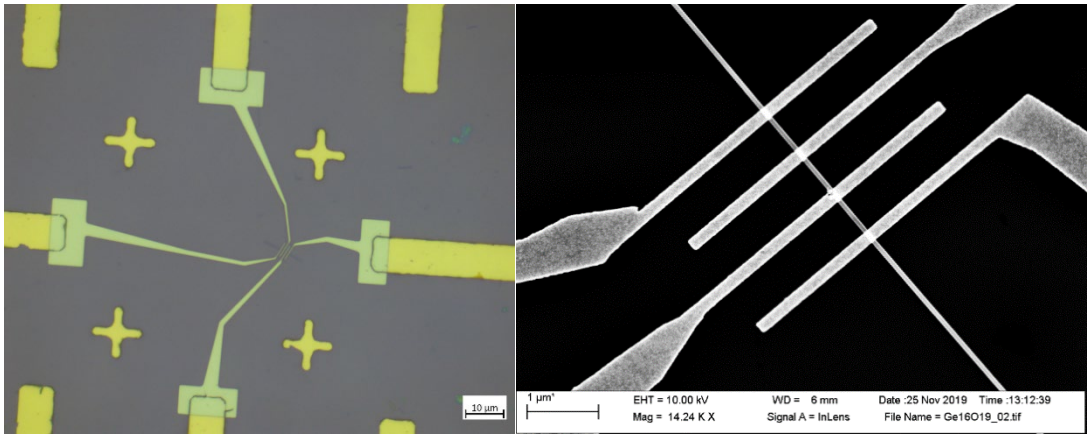

Figure 3.8: Ge NWs contacted for electrical testing shown to be intact after the electric fields had been applied.

The reasoning for the lack of electrical conductivity in the undoped NWs may be due to a higher incorporation of P into the Ge NWs than anticipated. The P/Ge ratios used were selected based on examples of gas-based CVD *in-situ* doping of Ge NWs in literature.[74,79,93] If the concentration of P within the NWs is above a certain threshold, the NWs will exhibit insulating behaviour, as seen here. Alternatively, the lack of control over the homogeneity of the P concentration throughout the NWs may result in clusters of P atoms throughout the crystal. Both of these will lead to an increase in scattering of electrons in the NWs. Once electrons travel within the scattering radius

around the P atoms, which have a positive charge after donating electrons as *n*-dopants, they are scattered, losing kinetic energy to a point where current is inhibited. Both an excessive P concentration and P clusters within the NWs could cause scattering, the former due to a large amount of scattering sites and the latter due to an increase in the scattering radii in the NWs. As no P clusters were observed via HRTEM, the former is the more likely of the two. However, as the undoped Ge NWs also showed insulating behaviour, it is likely that the issues with electrical testing of the NWs arose from issues associated with the contacting process, such as the ineffective removal of the Ge oxide layers for both the doped and undoped NW samples.

3.1.4 Summary of *in-situ* Doped Ge NWs

Overall, Ge NWs were successfully grown in the presence of three different dopant precursors, although each precursor had unique effects on NW growth. Though initial results were promising, especially for the TOP-doped NWs, unsuccessful electrical testing indicates that more work is required to optimise the *in-situ* doping of Ge NWs using liquid precursors.

3.2 *In situ* Doped CVD grown GeSn NWs

3.2.1 Microscopy of *In situ* Doped CVD grown GeSn NWs

In-situ doping experiments of GeSn NWs gave far less consistent results than with the Ge NWs, as can be seen in the SEM images shown in Figure 3.9. Undoped GeSn NWs grown under similar conditions to those previously reported by Biswas *et al.* [46] gave a sparser distribution across the Si substrate, giving a percentage coverage of

65.8 % as shown in Table 3.2. The NWs also exhibited a slight tapering, which may be attributed to the effects of Sn on the Au catalyst. EDX data shows NW tips to have a very high Sn concentration, thus it can be assumed that as the NW growth progressed, the Au seed absorbed Sn to such an extent that the seeds grew in size during the reaction as more Sn dissolved within them. Thus, as the seed-tip increased in size, the diameters of each bilayer of the NW increased, causing the tapering. Undoped wires had Sn concentrations of approximately 10 at. %, as shown in Figure 3.10.

Dopant precursors had a varied effect on the morphology of the NWs. NWs grown in the presence of DPP at 1.5 at. % were long and thin, more resembling Ge NWs than GeSn, though the substrate was as densely covered as the undoped GeSn samples, with both giving percentage coverage of approximately 65 %, as seen in Table 3.2. This is potentially due to the P atoms lowering the surface tension of the Au NPs, proposed by Schmid *et al.* as a factor affecting Si NW growth during P in *in-situ* doping.[82] This may also be the cause of the agglomerated Au particles present on the Si substrate in the SEM image in Figure 3.9. These NWs, with a resemblance to Ge NWs, had the highest Sn concentration at 80 at.% Sn. Although the NWs in this sample seemed promising candidates for FET applications, with this high Sn percentage, as well as the majority of NWs having diameters below 20 nm (as shown in Figure 3.11), they were highly unstable upon imaging by SEM and TEM, and were heavily damaged even by a low power SEM beam (see Figure 3.9(c)), and thus, STEM-EDX analysis of the NWs was unsuccessful. This unusual morphology, composition and structure of the GeSn NWs is potentially due the same effects of P from DPP on the surface tension of the Au seeds preventing Sn from dissolving into the seeds, and being

incorporated into the NW via the sidewalls. The instability of the NWs under electron beam is also unusual, as group IV NWs are generally highly stable under electron beam, and may be due to the effects of this sidewall deposition of Sn into the NW.

Although sparsely distributed across the substrate, NWs grown in the presence of DPP at a concentration of 0.5 at. % were more morphologically similar to undoped GeSn NWs. An increase in the Sn concentration was also observed here, though to a much lesser extent than the higher concentration DPP experiments, with Sn concentrations of around 15 at. %.

Table 3.2: Approximate percentage coverages of GeSn NWs on substrates taken from 12 μm^2 SEM images of NWs.

Dopant Precursor	**P/Ge at. % [1]**	**Percentage Coverage**
Undoped	-	65.8
DPP	1	64.9
DPP	0.2	53.2
TOP	1	91.9
TOP	0.2	63.6

1. Values calculated by measuring the percentage of SEM image composed of NWs via Java program written in-house that calculated the percentage of the image above a certain brightness in order to give an estimate of wire coverage.

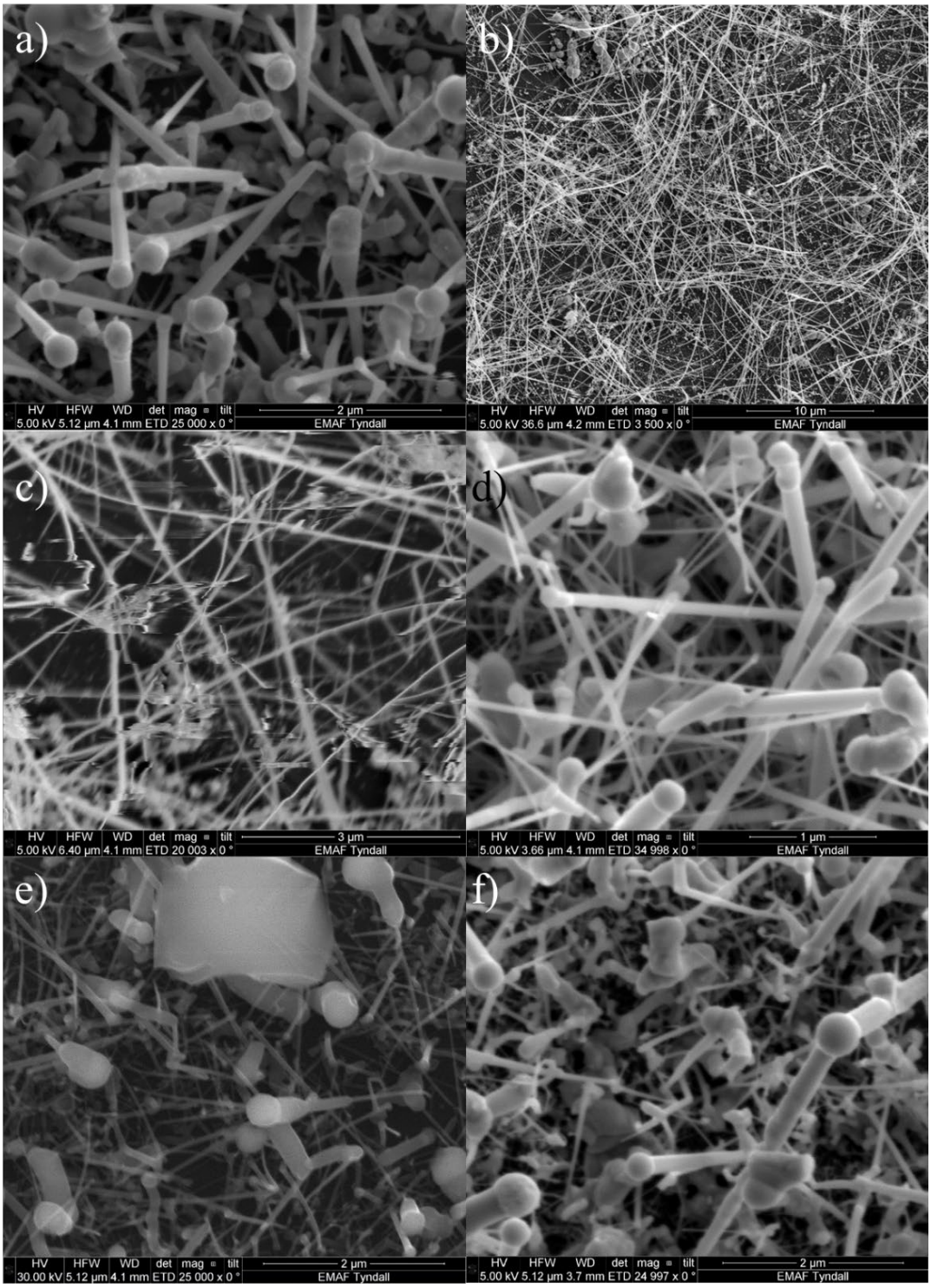

Figure 3.9: SEM images of *in-situ* doped GeSn NWs grown at differing concentrations of P-dopant precursors: (a) undoped, (b) 1.5 at. % P/Ge DPP, (c) 1.5 at. % DPP at higher magnification to show damage to NWs caused by electron beam (d) 0.5 at. % P/Ge DPP, (e) 1 at. % P/Ge TOP and (f) 0.2 at. % P/Ge TOP.

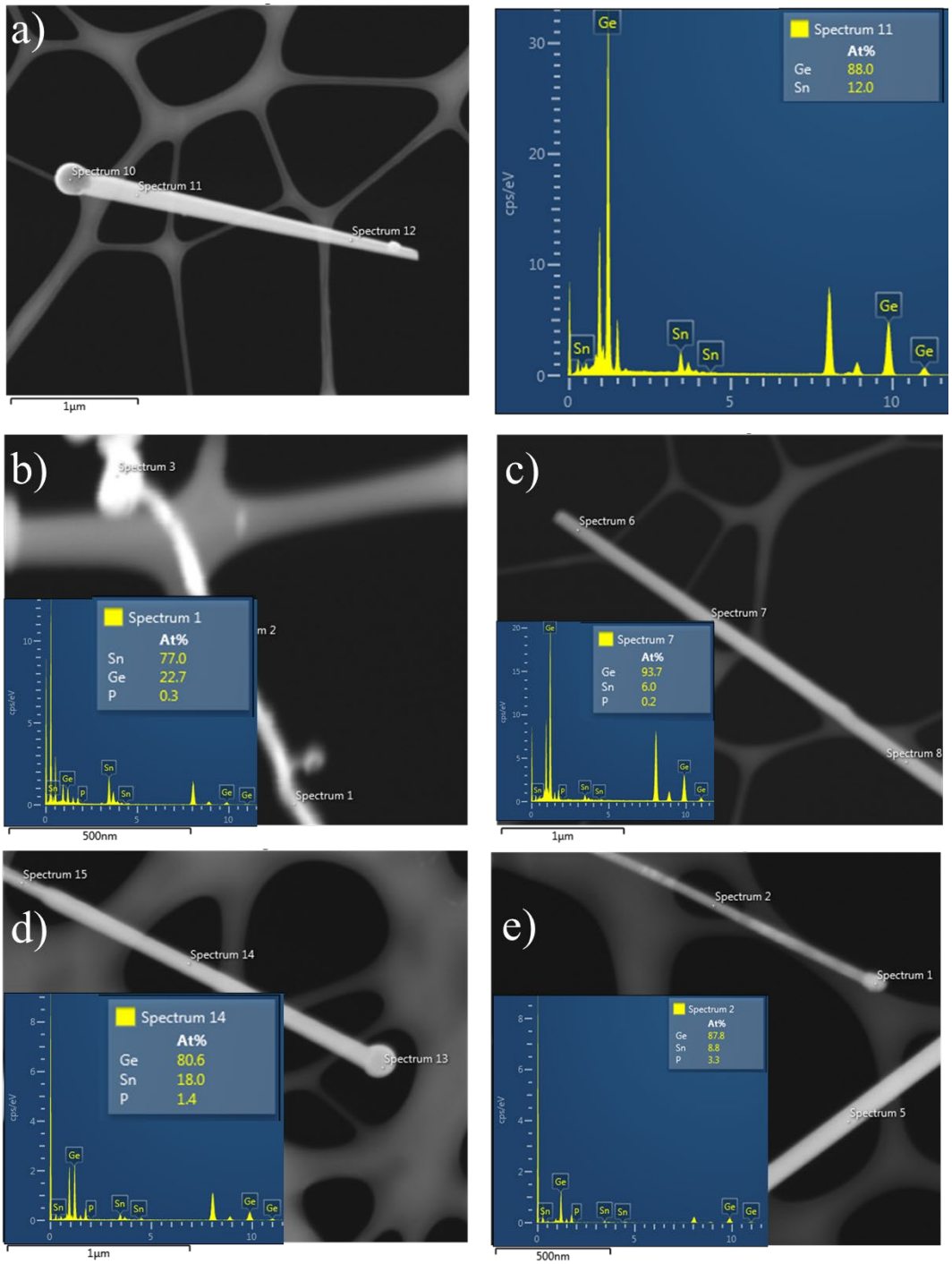

Figure 3.10: Point EDX spectra collected for *in-situ* doped GeSn NWs grown at differing concentrations of P-dopant precursors: (a) undoped, (b) 1.5 at. % DPP, (c) 0.5 at. %, DPP, (d) 1 at. % TOP and (e) 0.2 at. % TOP.

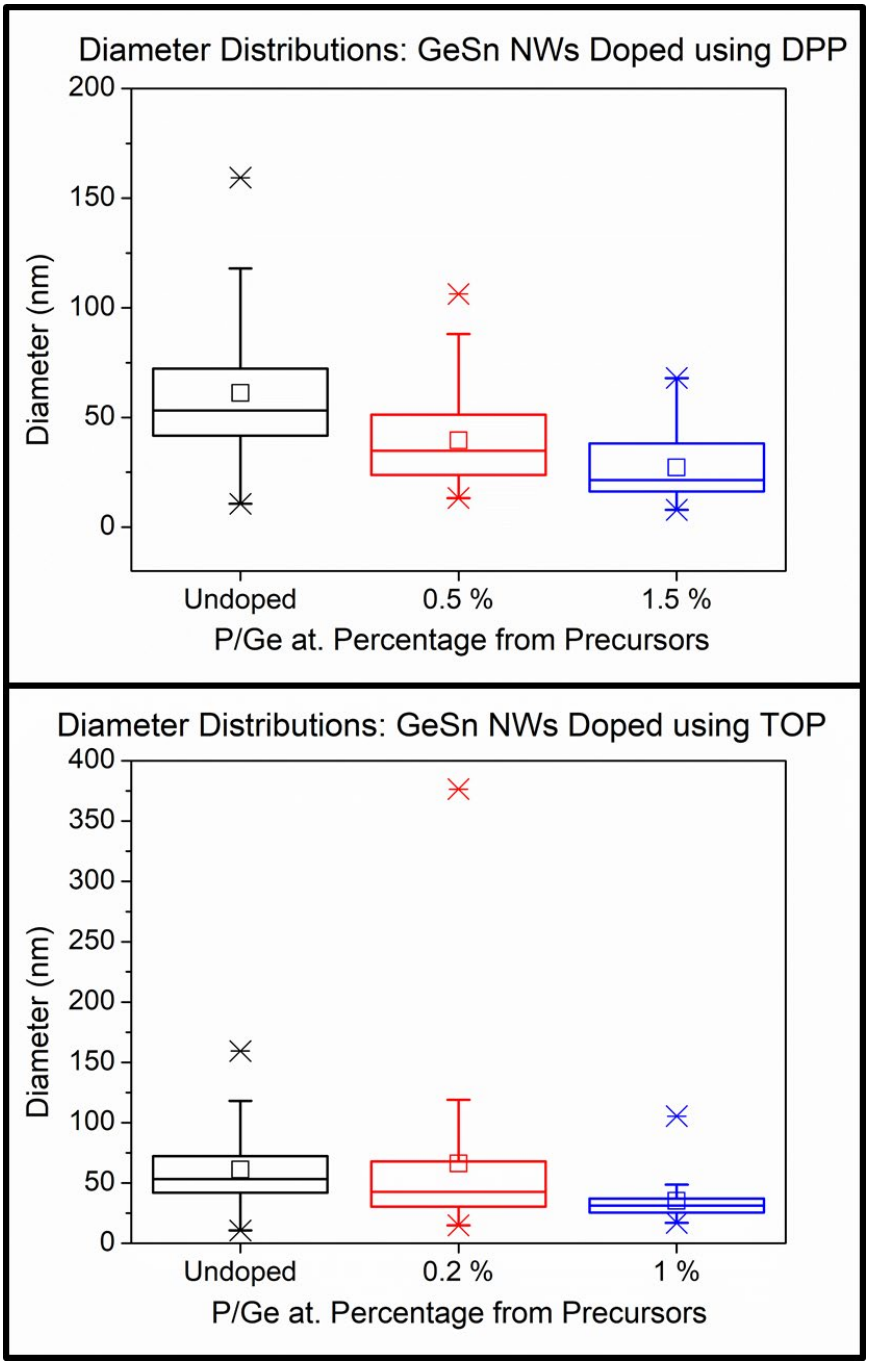

Figure 3.11: Box plots showing diameter distributions of *in-situ* doped and undoped GeSn NWs grown in the presence of different concentrations of dopant precursors.

Doped GeSn NWs grown using TOP as a precursor yielded samples that more closely resembled their undoped counterparts than those grown using other precursors. From SEM analysis, doped GeSn NWs grown using TOP as a precursor had similar mean diameters and morphologies to undoped NWs, although a slight variation in diameter

distributions and yields were apparent. However, the presence of TOP during the growth of GeSn NWs resulted in a lowering of the Sn concentration to 8 and 6 at.% for a TOP precursor concentration of 0.2 at. % and 1 at. % respectively, compared to 10 at.% for undoped GeSn NWs; probably due to interactions between TOP with the ATBS due to both molecules being based on alkyl chains rather than phenyl rings. At high TOP concentrations the GeSn NWs formed appeared to have a tight diameter distribution diameters (seen in Figure 3.11), with a mean diameter at around 30 nm.

3.2.2 Crystal Structures o*f In-situ* Doped CVD grown GeSn NWs

TEM analysis shown in Figure 3.12 of the GeSn NWs shows that undoped NWs, as well as NWs doped using TOP and 0.5 at. % P/Ge DPP, gave uniform crystal structures. Lattice spacings of 3.32 ± 0.08 Å was observed for the undoped sample, 3.29 ± 0.05 Å for the 1 at. % and 0.2 at. % TOP doped samples, and 3.29 ± 0.04 Å for the 0.25 at % P/Ge DPP doped sample, indicating that all NW grow in the (111) direction. The TEM image of the 1.5 at. % P/Ge doped DPP sample in Figure 3.13 shows that NWs contained many crystal defects, and inhomogeneous crystal structure. This is possibly the cause of the instability of the NWs under electron beam, and may be a result of the effects of P on the surface tension and composition of the liquid Au seeds during growth. XRD measurements undertaken on doped and undoped GeSn NWs proved that almost all samples had cubic crystal structures, with lattice spacings of 3.28 Å for undoped GeSn NWs and 3.29 Å for 0.5 at. % Ge/P DPP and both TOP doped samples. Most samples exhibited strong (111), (220), (311) and less intense (400) and (331) diffraction peaks from Ge (see Figure 3.14). The exception again is the 1.5 at. % DPP sample, which showed only weak peaks at around 28 and 49° (2θ). The Raman spectra shown in Figure 3.15 shows the cubic Ge-Ge peak at 300 cm^{-1} for

all samples. This peak has a noticeable red-shift for the undoped and 0.2 at. % Ge/P TOP doped sample, which is expected, due to the presence of the heavier Sn atoms in the NWs. All samples also show a peak at 435 cm^{-1}, potentially giving evidence of P-doping. However, the low intensities of most of the spectra before being normalised render this peak unreliable. Unusual spectra were seen for 1.5 at. % DPP samples, with peaks at 230 and 250 cm^{-1}. As these NWs are more highly composed of Sn, these peaks are most likely due to Sn_xO_y oxide peaks, as seen in previous Raman studies of Sn oxides.[123,124] There is also a noticeable blue-shift in the Ge peak at around 300 cm^{-1} when compared to all other samples, the implication here being that Sn has segregated onto the surface of the NWs and formed oxides, while the NWs themselves are mainly composed of Ge, giving evidence of DPP causing radial deposition of Sn on the surface of the NWs. All data confirms that NWs are cubic, and indicates the instability of DPP as a P-dopant precursor in high concentrations. As with the Ge NWs, some samples show peaks at 30 and 32° (2θ), indicating tetragonal NWs. However, as neither TEM nor Raman gave any evidence of this, these peaks can be assumed to be unrelated to the GeSn NWs. This again is likely due to peaks from the Si substrate..

From these experiments the P precursors appear to have a greater effect on defects, morphology, and compositions of GeSn NWs compared to their Ge counterparts. There is a possibility that entirely new precursors must be considered for GeSn NWs, based on the instability, lowering of Sn concentrations and potential inefficient doping of the wires formed here.

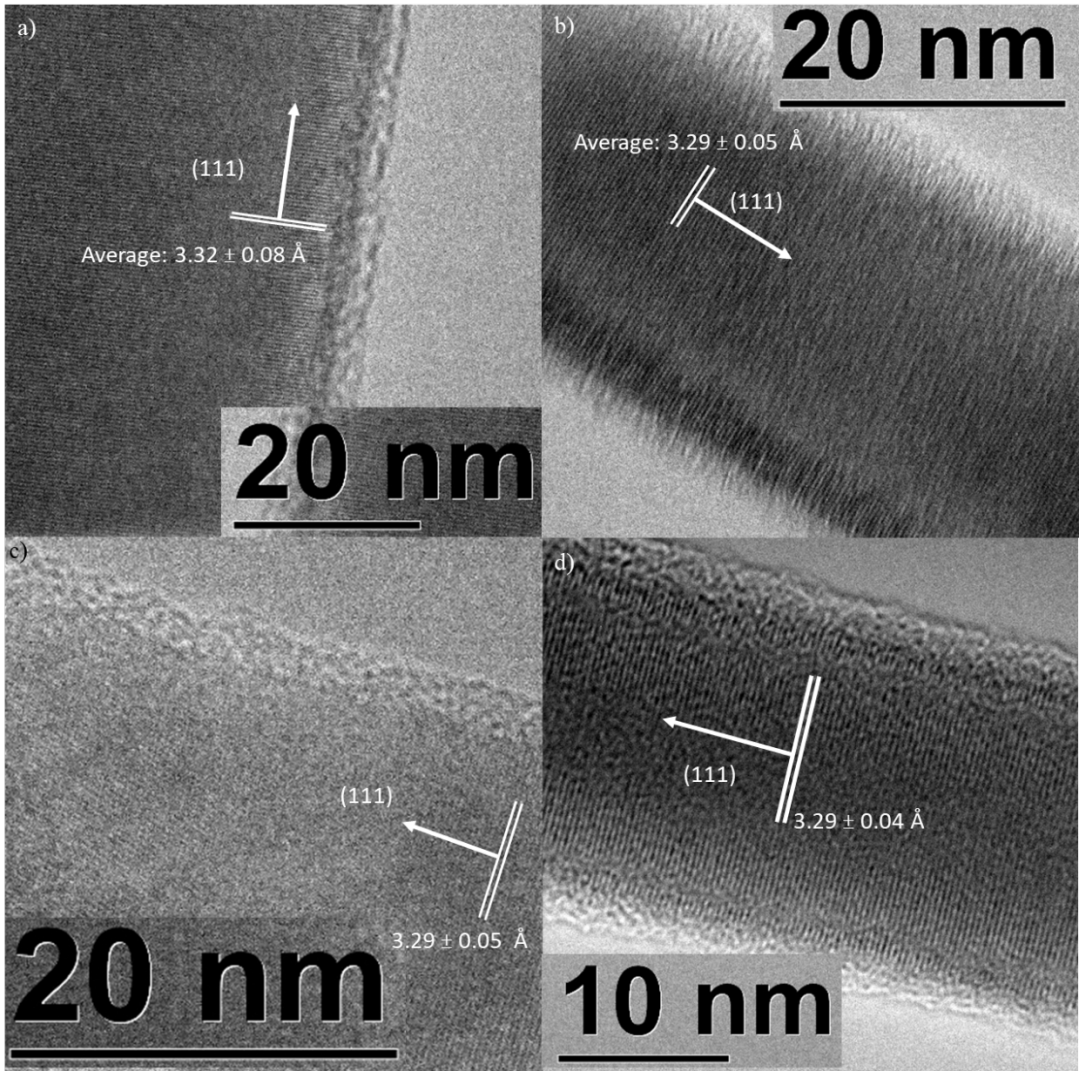

Figure 3.12: TEM images of *in-situ* doped GeSn NWs grown at differing concentrations of P-dopant precursors: (a) undoped, (b) 0.2 at. %, TOP, (c) 1 at. % TOP and (d) 0.25 at. % DPP.

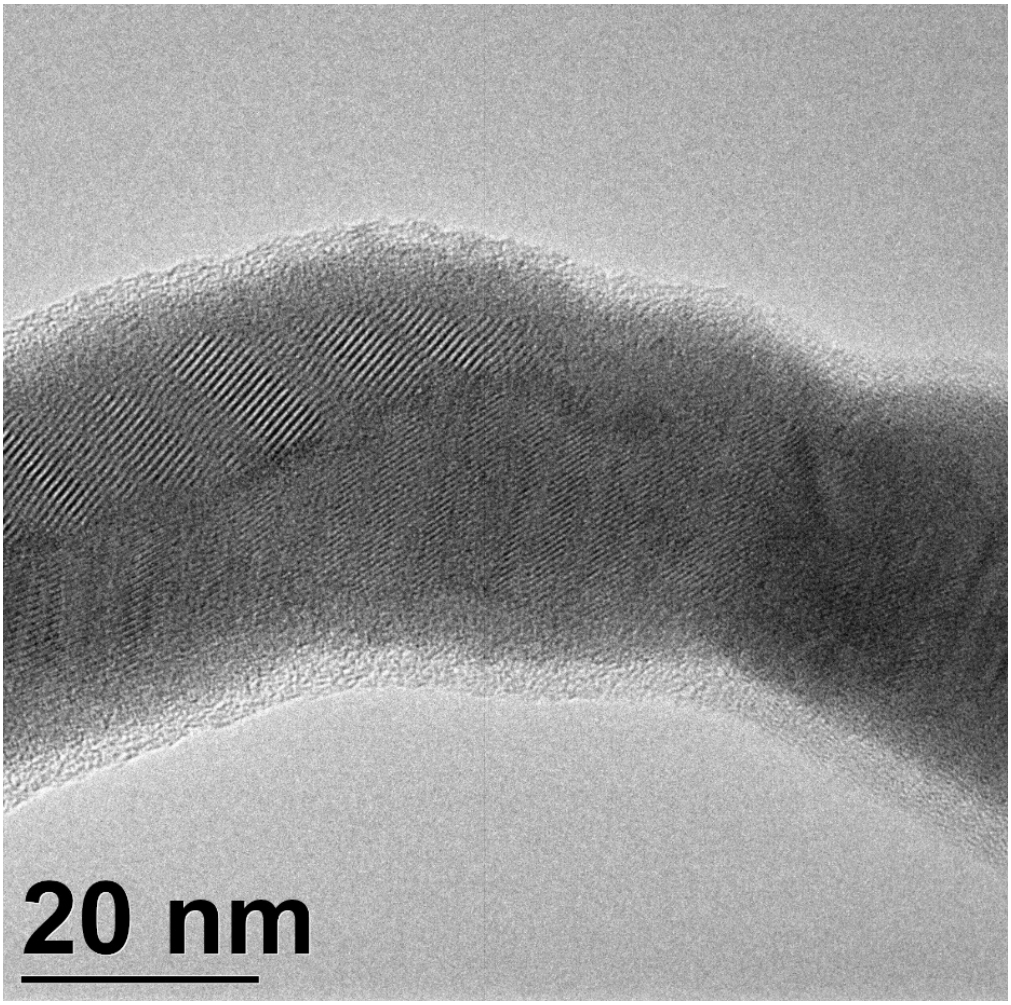

Figure 3.13: TEM image of *in-situ* doped GeSn NWs doped using 1.5 at. % P/Ge DPP, showing defects in the crystal structure.

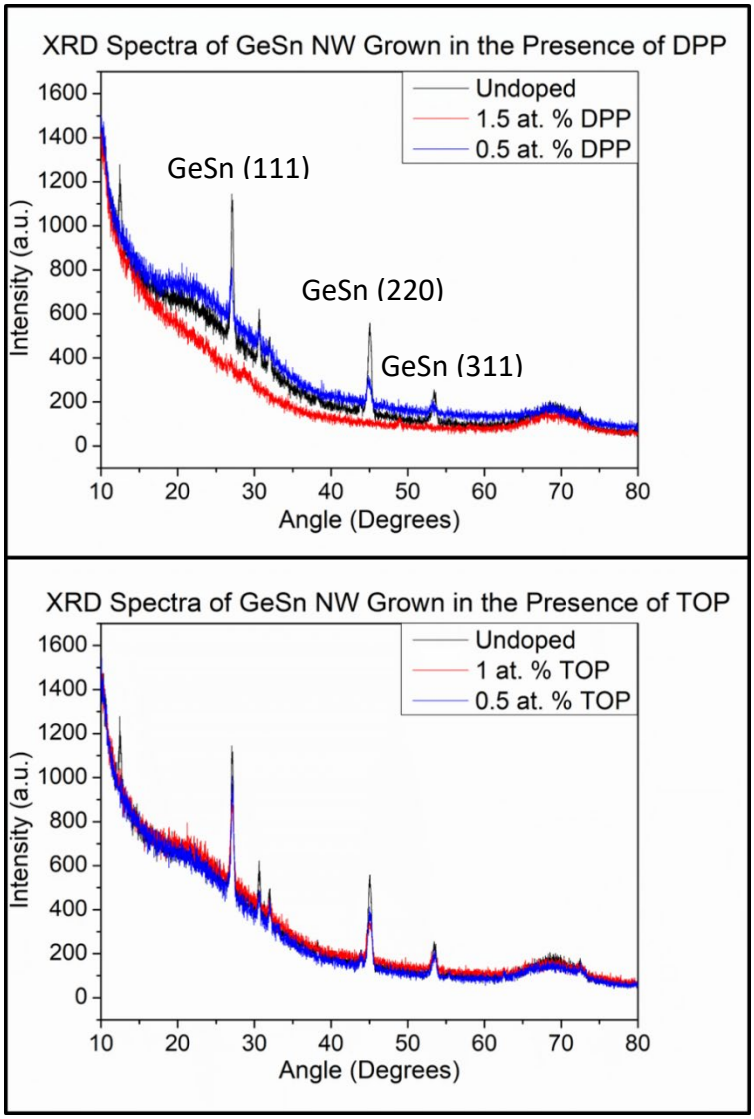

Figure 3.14: XRD Spectra of of *in situ* doped GeSn NWs grown in the presence of different concentrations of each dopant-precursor. Peaks labelled in DPP spectra as measured by Zaima *et al.*[125]

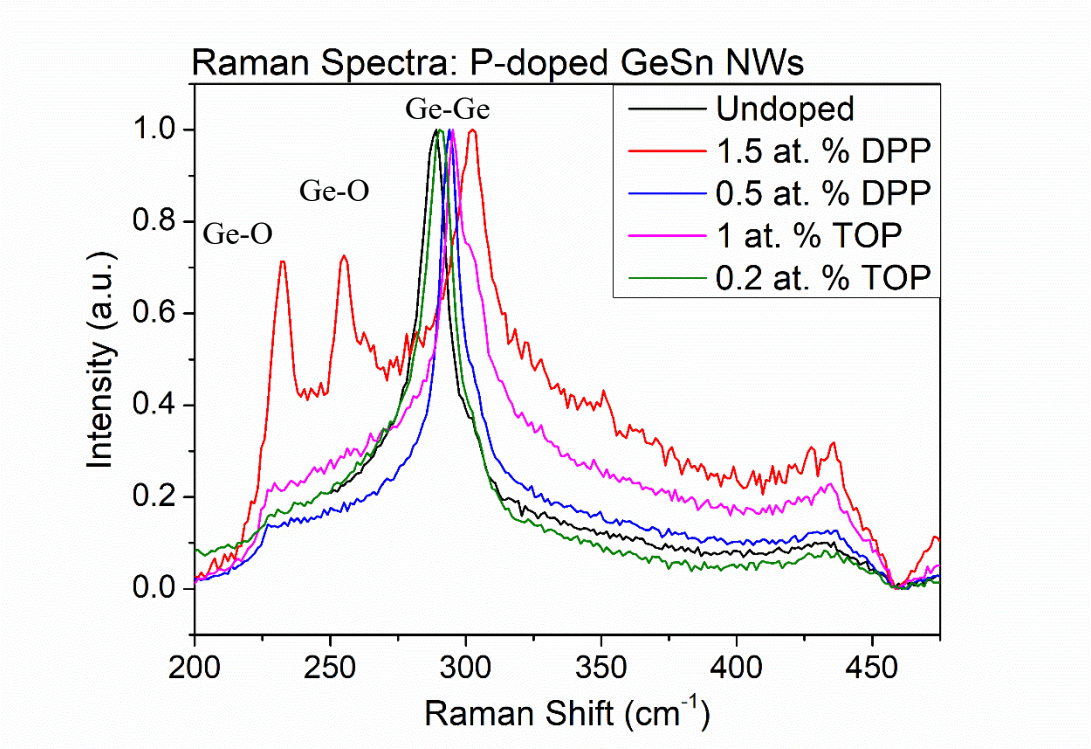

Figure 3.15: Raman Spectra of of *in-situ* doped GeSn NWs grown at differing concentrations of P-dopant precursors.

3.2.3 Electrical results of *in-situ* doped GeSn NWs

The electrical testing of the doped GeSn NWs gave unusual results. While GeSn NWs synthesised within our group have given promising and expected electrical behaviour, the TOP-doped GeSn NWs gave highly unconventional IV curves when altering the drain voltage, and backgate voltage. Although current modulation occurred in some cases, other NWs gave current peaks in the μA scale that then dropped to the nA scale, giving a modulation in current. Figure 3.16 shows electrical results for GeSn NWs doped at 1 and 0.2 at. % P/Ge ((a) and (b), respectively). This bizarre behaviour, and generally low current may be explained by a limit of the current due to scattering sites within the NWs, as seen in literature with ion-implanted bulk Si,[126,127] and is prone to occur in NWs.[128] These are caused by clusters of dopant atoms forming defects in interstitial sites rather than becoming part of the crystal structure, and prevent electrons from passing through the NWs effectively. This may be avoided, as in literature by

thermally annealing the NWs, to ensure that the dopant atoms form part of the crystal structure rather than in intestinal sites to form defects. However, difficulty lies here in annealing the NWs without causing segregation of the Sn atoms. It may also be prevented in future by further lowering the dopant concentration, or altering the flow rate of P into the reaction vessel to better control the distribution of P in the NWs.

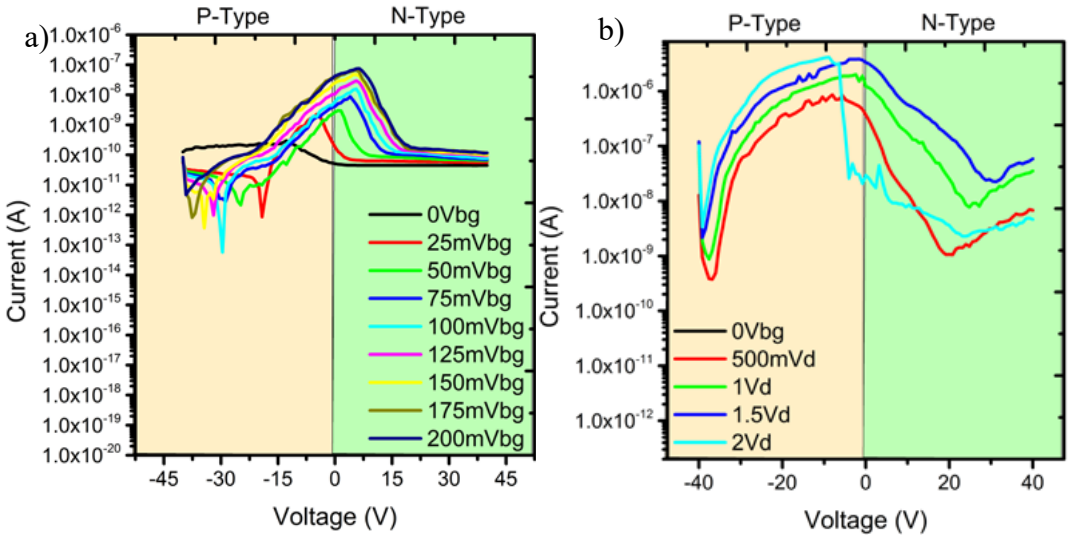

Figure 3.16: IV curves of GeSn NWs doped using TOP as dopant precursor, with differing backgate voltage and drain voltage, as outlined in each figure. (a) and (b) show 1 and 0.2 at. % P/Ge doped GeSn NWs, respectively.

Conclusions and Future Work

This study showed the successful synthesis of Ge and GeSn NWs using solution-based VLS growth in the presence of P precursors. While it was established that none of the P precursors affected the crystal structure, with all doped NWs showing cubic crystal structures, and growing in the (111) direction, the yields of the wires were shown to have decreased with dopant precursors present, attributed here to the effects of P on the Au seed system, with both the effects of P in decreasing the growth velocity, and the potential lowering of the Au seed surface tension. In the case of Ge NWs, TOP proved to be the optimum dopant precursor in terms of NW morphology and yield. P

precursors had a greater impact on the GeSn NWs, where EDX and Raman Spectroscopy showed that they widely altered the concentration of Sn present in each sample, as well as TEM images showing changes in the crystal structures in of the NWs doped using higher concentrations of DPP. In spite of these setbacks, the results from the peak present at around 435 cm^{-1} and Fano Broadening of the 300 cm^{-1} Ge peak in the Raman spectra give evidence of successful P doping of the NWs.

Electrical results have shown that these doped NWs need significant work before their use in FETs. The unconventional electrical behaviour of the doped GeSn NWs indicates that scattering sites have occurred as part of the doping process, preventing the NWs from acting as effective channels. As well as this, no current was detected in the Ge NWs, also attributed to scattering sites here. While annealing may be effective for resolving this in bulk semiconductors, this may result in either the melting of the NWs, or Sn segregation in the GeSn NWs. Thus, possible solutions would involve altering the growth of the NWs, potentially by using metal NPs as catalysts to increase the growth velocity by lowering the equilibrium concentrations of the NWs. Thus, fewer atoms of P would be incorporated into the NWs, potentially preventing the scattering sites from forming. As well as this, the process for electrically testing solution-based VLS-grown *in-situ* doped Ge and GeSn NWs needs further refinement.

Once these initial problems have been navigated, work may continue into the doping of GeSn NWs for use in tFETs, which will involve heterogeneously doping the NWs to form *p-i-n* junctions. However, as has been shown here, *in-situ* doping of Ge and GeSn NWs using solution-based precursors is far from trivial and more research is necessary to refine the integration of dopants into the crystal structures of the NWs.

References

(1) Moore, G. E. Cramming More Components onto Integrated Circuits. *Electronics* **1965**, *38* (8), 114–117.

(2) Shilov, A. Intel Q3 2019 Fab Update: 10nm Product Era Has Begun, 7 nm On Track https://www.anandtech.com/show/15032/intel-2019-fab-update-10nm-hvm-7nm-on-track (accessed Jan 16, 2020).

(3) ExtremeTech. Computing. https://www.extremetech.com/computing/291029-intel-will-launch-7nm-chips-in-2021-ice-lake-ships-in-june (accessed Jan 16, 2020).

(4) Techradar. https://www.techradar.com/news/amd-navi (accessed Jan 16, 2020).

(5) International Technology Roadmap for Semiconductors 2.0 (ITRS2. 0). Semiconductor Industry Association; 2015.

(6) Li, W.; Ning, H.; Yu, Z.; Shi, Y.; Wang, X. Reducing the Power Consumption of Two-Dimensional Logic Transistors. *J. Semicond.* **2019**, *40* (9), 091002.

(7) Bin Yu; Leland Chang; Ahmed, S.; Haihong Wang; Bell, S.; Chih-Yuh Yang; Tabery, C.; Chau Ho; Qi Xiang; Tsu-Jae King; et al. FinFET Scaling to 10 Nm Gate Length. In *Digest. International Electron Devices Meeting,*; IEEE: San Fransisco, CA, USA, 2002; pp 251–254.

(8) Riordan, M.; Hoddeson, L.; Herring, C. The Invention of the Transistor. *Rev. Mod. Phys.* **1999**, *71* (2), S336-345.

(9) Sun, C.; Liang, R.; Liu, L.; Wang, J.; Xu, J. Leakage Current of Germanium-on-Insulator-Based Junctionless Nanowire Transistors. *Appl. Phys. Lett.* **2015**, *107* (13), 132105.

(10) Claeys, C.; Mitard, J.; Eneman, G.; Meuris, M.; Simoen, E. Si versus Ge for Future Microelectronics. *Thin Solid Films* **2010**, *518* (9), 2301–2306.

(11) Yoon, Y. J.; Seo, J. H.; Cho, S.; Kwon, H. I.; Lee, J. H.; Kang, I. M. Sub-10 Nm Ge/GaAs Heterojunction-Based Tunneling Field-Effect Transistor with Vertical Tunneling Operation for Ultra-Low-Power Applications. *J. Semicond. Technol. Sci.*

2016, *16* (2), 172–178.

(12) Yu, R.; Georgiev, Y. M.; Das, S.; Hobbs, R. G.; Povey, I. M.; Petkov, N.; Shayesteh, M.; O'Connell, D.; Holmes, J. D.; Duffy, R. Junctionless Nanowire Transistor Fabricated with High Mobility Ge Channel. *Phys. Status Solidi - Rapid Res. Lett.* **2014**, *8* (1), 65–68.

(13) Sau, J. D.; Cohen, M. L. Possibility of Increased Mobility in Ge-Sn Alloy System. *Phys. Rev. B - Condens. Matter Mater. Phys.* **2007**, *75* (4), 1–7.

(14) Liu, M.; Liu, Y.; Wang, H.; Zhang, Q.; Zhang, C.; Hu, S.; Hao, Y.; Han, G. Design of GeSn-Based Heterojunction-Enhanced N-Channel Tunneling FET with Improved Subthreshold Swing and ON-State Current. *IEEE Trans. Electron Devices* **2015**, *62* (4), 1262–1268.

(15) Del Alamo, J. A. Nanometer-Scale InGaAs Field-Effect Transistors for THz and CMOS Technologies. In *European Solid-State Device Research Conference*; IEEE Computer Society: Cambridge, MA, USA, 2013; pp 16–21.

(16) Jain, F.; Karmakar, S.; Chan, P. Y.; Suarez, E.; Gogna, M.; Chandy, J.; Heller, E. Quantum Dot Channel (QDC) Field-Effect Transistors (FETs) Using II-VI Barrier Layers. *J. Electron. Mater.* **2012**, *41* (10), 2775–2784.

(17) Collaert, N.; De Keersgieter, A.; Dixit, A.; Ferain, I.; Lai, L. S.; Lenoble, D.; Mercha, A.; Nackaerts, A.; Pawlak, B. J.; Rooyackers, R.; et al. Multi-Gate Devices for the 32 Nm Technology Node and Beyond. *Solid. State. Electron.* **2008**, *52* (9), 1291–1296.

(18) Hisamoto, D.; Lee, W.; Kedzierski, J.; Takeuchi, H.; Asano, K.; Kuo, C.; Anderson, E.; King, T.; Bokor, J.; Hu, C. FinFET — A Self-Aligned Double-Gate MOSFET. **2000**, *47* (12), 2320–2325.

(19) Gola, D.; Singh, B.; Singh, J.; Jit, S.; Tiwari, P. K. Static and Quasi-Static Drain Current Modeling of Tri-Gate Junctionless Transistor with Substrate Bias-Induced Effects. *IEEE Trans. Electron Devices* **2019**, *66* (7), 2876–2883.

(20) Park, J.; Colinge, J.; Diaz, C. H.; Member, S. Pi-Gate SOI MOSFET. *IEEE Electron Device Lett.* **2001**, *22* (8), 405–406.

(21) Colinge, J.-P.; Lee, C.-W.; Afzalian, A.; Akhavan, N. D.; Yan, R.; Ferain, I.; Razavi, P.; O'Neill, B.; Blake, A.; White, M.; Kelleher, A-M.; McCarthy, B.; Murphy, R. Nanowire Transistors without Junctions. *Nat. Nanotechnol.* **2010**, *5* (3), 225–229.

(22) Park, C. H.; Ko, M. D.; Kim, K. H.; Baek, R. H.; Sohn, C. W.; Baek, C. K.; Park, S.; Deen, M. J.; Jeong, Y. H.; Lee, J. S. Electrical Characteristics of 20-Nm Junctionless Si Nanowire Transistors. *Solid. State. Electron.* **2012**, *73*, 7–10.

(23) Lou, H.; Zhang, L.; Zhu, Y.; Lin, X.; Yang, S.; He, J.; Chan, M. A Junctionless Nanowire Transistor with a Dual-Material Gate. *IEEE Trans. Electron Devices* **2012**, *59* (7), 1829–1836.

(24) Björk, M. T.; Knoch, J.; Schmid, H.; Riel, H.; Riess, W. Silicon Nanowire Tunneling Field-Effect Transistors. *Appl. Phys. Lett.* **2008**, *92* (19), 193504.

(25) Moselund, K. E.; Schmid, H.; Bessire, C.; Bjork, M. T.; Ghoneim, H.; Riel, H. InAs-Si Nanowire Heterojunction Tunnel FETs. *IEEE Electron Device Lett.* **2012**, *33* (10), 1453–1455.

(26) Hraziia; Vladimirescu, A.; Amara, A.; Anghel, C. An Analysis on the Ambipolar Current in Si Double-Gate Tunnel FETs. *Solid. State. Electron.* **2012**, *70*, 67–72.

(27) Wagner, R. S.; Ellis, W. C. Vapor-Liquid-Solid Mechanism of Single Crystal Growth. *Appl. Phys. Lett.* **1964**, *4* (5), 89–90.

(28) Chen, L.; Lu, W.; Lieber, C. M. Chapter 1. Semiconductor Nanowire Growth and Integration. In *RSC Smart Materials*; 2015; pp 1–53.

(29) Singh, N.; Buddharaju, K. D.; Manhas, S. K.; Agarwal, A.; Rustagi, S. C.; Lo, G. Q.; Balasubramanian, N.; Kwong, D. L. Si, SiGe Nanowire Devices by Top-down Technology and Their Applications. *IEEE Trans. Electron Devices* **2008**, *55* (11), 3107–3118.

(30) Hobbs, R. G.; Petkov, N.; Holmes, J. D. Semiconductor Nanowire Fabrication by Bottom-up and Top-down Paradigms. *Chem. Mater.* **2012**, *24* (11), 1975–1991.

(31) Sun, Y.; Graff, R. A.; Strano, M. S.; Rogers, J. A. Top-down Fabrication of Semiconductor Nanowires with Alternating Structures along Their Longitudinal and

Transverse Axes. *Small* **2005**, *1* (11), 1052–1057.

(32) Maas, D.; van Veldhoven, E.; Chen, P.; Sidorkin, V.; Salemink, H.; van der Drift, E.; Alkemade, P. Nanofabrication with a Helium Ion Microscope. In *Metrology, Inspection, and Process Control for Microlithography XXIV*; Raymond, C. J., Ed.; San Jose, CA, USA, 2010; Vol. 7638, p 763814.

(33) Mårtensson, T.; Carlberg, P.; Borgström, M.; Montelius, L.; Seifert, W.; Samuelson, L. Nanowire Arrays Defined by Nanoimprint Lithography. *Nano Lett.* **2004**, *4* (4), 699–702.

(34) Gentile, P.; Solanki, A.; Pauc, N.; Oehler, F.; Salem, B.; Rosaz, G.; Baron, T.; Den Hertog, M.; Calvo, V. Effect of HCl on the Doping and Shape Control of Silicon Nanowires. *Nanotechnology* **2012**, *23* (21), 215702.

(35) Kim, S.; Hill, D. J.; Pinion, C. W.; Christesen, J. D.; McBride, J. R.; Cahoon, J. F. Designing Morphology in Epitaxial Silicon Nanowires: The Role of Gold, Surface Chemistry, and Phosphorus Doping. *ACS Nano* **2017**, *11* (5), 4453–4462.

(36) Quitoriano, N. J.; Wu, W.; Kamins, T. I. Guiding Vapor-Liquid-Solid Nanowire Growth Using SiO2. *Nanotechnology* **2009**, *20* (14), 145303.

(37) Sivakov, V. A.; Scholz, R.; Syrowatka, F.; Falk, F.; Gosele, U.; Christiansen, S. H. Silicon Nanowire Oxidation: The Influence of Sidewall Structure and Gold Distribution. *Nanotechnology* **2009**, *20* (40), 405607.

(38) Ganjipour, B.; Wallentin, J.; Borgström, M. T.; Samuelson, L.; Thelander, C. Tunnel Field-Effect Transistors Based on InP-GaAs Heterostructure Nanowires. *ACS Nano* **2012**, *6* (4), 3109–3113.

(39) Verheijen, M. A.; Immink, G.; de Smet, T.; Borgström, M. T.; Bakkers, E. P. A. M. Growth Kinetics of Heterostructured GaP−GaAs Nanowires. *J. Am. Chem. Soc.* **2006**, *128* (4), 1353–1359.

(40) Persson, A. I.; Larsson, M. W.; Stenstrom, S.; Ohlsson, B. J.; Samuelson, L.; Wallenberg, L. R. Solid-Phase Diffusion Mechanism for GaAs Nanowire Growth. *Nat Mater* **2004**, *3* (10), 677–681.

(41) Wang, Y.; Schmidt, V.; Senz, S.; Gösele, U. Epitaxial Growth of Silicon Nanowires Using an Aluminium Catalyst. *Nat. Nanotechnol.* **2006**, *1* (3), 186–189.

(42) Mullane, E.; Kennedy, T.; Geaney, H.; Dickinson, C.; Ryan, K. M. Synthesis of Tin Catalyzed Silicon and Germanium Nanowires in a Solvent-Vapor System and Optimization of the Seed/Nanowire Interface for Dual Lithium Cycling. *Chem. Mater.* **2013**, *25* (9), 1816–1822.

(43) Chockla, A. M.; Harris, J. T.; Korgel, B. A. Colloidal Synthesis of Germanium Nanorods. *Chem. Mater.* **2011**, *23* (7), 1964–1970.

(44) Sun, X. H.; Didychuk, C.; Sham, T. K.; Wong, N. B. Germanium Nanowires: Synthesis, Morphology and Local Structure Studies. *Nanotechnology* **2006**, *17* (12), 2925–2930.

(45) Morales, A.M and Lieber, C. M. A Laser Ablation Method for the Synthesis of Crystalline Semiconductor Nanowires. *Science* **1998**, *279* (5348), 208–211.

(46) Biswas, S.; Doherty, J.; Saladukha, D.; Ramasse, Q. M.; Majumdar, D.; Upmanyu, M.; Singha, A.; Ochalski, T.; Morris, M. A.; Holmes, J. D. Non-Equlilbrium Induction of Tin in Germanium: Towards Direct Bandgap $Ge_{1-x}Sn_x$ Nanowires. *Nat. Commun.* **2016**, *7* (110406).

(47) Trentler, T. J.; Hickman, K. M.; Goel, S. C.; Viano, A. M.; Gibbons, P. C.; Buhro, W. E. Solution-Liquid-Solid Growth of Crystalline III-V Semiconductors: An Analogy to Vapor-Liquid-Solid Growth. *Science (80-.).* **1995**, *270* (5243), 1791–1794.

(48) Chockla, A. M.; Korgel, B. A. Seeded Germanium Nanowire Synthesis in Solution. *J. Mater. Chem.* **2009**, *19* (7), 996–1001.

(49) Hanrath, T.; Korgel, B. A. Supercritical Fluid-Liquid-Solid (SFLS) Synthesis of Si and Ge Nanowires Seeded by Colloidal Metal Nanocrystals. *Adv. Mater.* **2003**, *15* (5), 437–440.

(50) Schricker, A. D.; Joshi, S. V.; Hanrath, T.; Banerjee, S. K.; Korgel, B. A. Temperature Dependence of the Field Effect Mobility of Solution-Grown

Germanium Nanowires. *J. Phys. Chem. B* **2006**, *110* (13), 6816–6823.

(51) Wang, Y.; Schmidt, V.; Senz, S.; Gösele, U. Epitaxial Growth of Silicon Nanowires Using an Aluminium Catalyst. *Nat. Nanotechnol.* **2006**, *1* (3), 186–189.

(52) Lotty, O.; Hobbs, R.; O'Regan, C.; Hlina, J.; Marschner, C.; O'Dwyer, C.; Petkov, N.; Holmes, J. D. Self-Seeded Growth of Germanium Nanowires: Coalescence and Ostwald Ripening. *Chem. Mater.* **2013**, *25* (2), 215–222.

(53) Colinge, J. P. Multi-Gate SOI MOSFETs. *Microelectron. Eng.* **2007**, *84* (9–10), 2071–2076.

(54) Longo, R. C.; Mattson, E. C.; Vega, A.; Cabrera, W.; Cho, K.; Chabal, Y. J.; Thissen, P. Mechanism of Arsenic Monolayer Doping of Oxide-Free Si(111). *Chem. Mater.* **2016**, *28* (7), 1975–1979.

(55) Longo, R. C.; Cho, K.; Hohmann, S.; Thissen, P. Mechanism of Phosphorus Transport Through Silicon Oxide during Phosphonic Acid Monolayer Doping. *J. Phys. Chem. C* **2018**, *122* (18), 10088–10095.

(56) Alphazan, T.; Mathey, L.; Schwarzwälder, M.; Lin, T. H.; Rossini, A. J.; Wischert, R.; Enyedi, V.; Fontaine, H.; Veillerot, M.; Lesage, A.; Emsley, L.; Veyre, L.; Martin, F.; Thieuleux, C.; Copéret, C. Monolayer Doping of Silicon through Grafting a Tailored Molecular Phosphorus Precursor onto Oxide-Passivated Silicon Surfaces. *Chem. Mater.* **2016**, *28* (11), 3634–3640.

(57) Ho, J. C.; Yerushalmi, R.; Jacobson, Z. A.; Fan, Z.; Alley, R. L.; Javey, A. Controlled Nanoscale Doping of Semiconductors via Molecular Monolayers. *Nat. Mater.* **2008**, *7* (1), 62–67.

(58) Cho, K.; Ruebusch, D. J.; Lee, M. H.; Moon, J. H.; Ford, A. C.; Kapadia, R.; Takei, K.; Ergen, O.; Javey, A. Molecular Monolayers for Conformal, Nanoscale Doping of InP Nanopillar Photovoltaics. *Appl. Phys. Lett.* **2011**, *98* (20), 3–5.

(59) Mattson, E. C.; Chabal, Y. J. Understanding Thermal Evolution and Monolayer Doping of Sulfur-Passivated GaAs(100). *J. Phys. Chem. C* **2018**, *122* (15), 8414–8422.

(60) Usami, A.; Ando, M.; Tsunekane, M.; Wada, T. Shallow-Junction Formation on Silicon by Rapid Thermal Diffusion of Impurities from a Spin-on Source. *IEEE Trans. Electron Devices* **1992**, *39* (1), 105–110.

(61) Hazut, O.; Agarwala, A.; Amit, I.; Subramani, T.; Zaidiner, S.; Rosenwaks, Y.; Yerushalmi, R. Contact Doping of Silicon Wafers and Nanostructures with Phosphine Oxide Monolayers. *ACS Nano* **2012**, *6* (11), 10311–10318.

(62) Hazut, O.; Huang, B. C.; Pantzer, A.; Amit, I.; Rosenwaks, Y.; Kohn, A.; Chang, C. S.; Chiu, Y. P.; Yerushalmi, R. Parallel p-n Junctions across Nanowires by One-Step Ex Situ Doping. *ACS Nano* **2014**, *8* (8), 8357–8362.

(63) Ingole, S.; Aella, P.; Manandhar, P.; Chikkannanavar, S. B.; Akhadov, E. A.; Smith, D. J.; Picraux, S. T. Ex Situ Doping of Silicon Nanowires with Boron. *J. Appl. Phys.* **2008**, *103* (10).

(64) Haraguchi, K.; Katsuyama, T.; Hiruma, K.; Ogawa, K. GaAs p-n Junction Formed in Quantum Wire Crystals. *Appl. Phys. Lett.* **1992**, *60* (6), 745–747.

(65) Greytak, A. B.; Lauhon, L. J.; Gudiksen, M. S.; Lieber, C. M. Growth and Transport Properties of Complementary Germanium Nanowire Field-Effect Transistors. *Appl. Phys. Lett.* **2004**, *84* (21), 4176–4178.

(66) Sun, Z.; Hazut, O.; Huang, B. C.; Chiu, Y. P.; Chang, C. S.; Yerushalmi, R.; Lauhon, L. J.; Seidman, D. N. Dopant Diffusion and Activation in Silicon Nanowires Fabricated by Ex Situ Doping: A Correlative Study via Atom-Probe Tomography and Scanning Tunneling Spectroscopy. *Nano Lett.* **2016**, *16* (7), 4490–4500.

(67) Cai, Y.; Camacho-Aguilera, R.; Bessette, J. T.; Kimerling, L. C.; Michel, J. High Phosphorous Doped Germanium: Dopant Diffusion and Modeling. *J. Appl. Phys.* **2012**, *112* (3), 1–6.

(68) Islam, M. S.; Mehedi, I. M. Comparative Study of the Effects of Phosphorus and Boron Doping in Vapor–Liquid–Solid Growth with Fixed Flow of Silicon Gas. *J. Cryst. Growth* **2016**, *440*, 55–61.

(69) Wallentin, J.; Borgström, M. T. Doping of Semiconductor Nanowires. *J. Mater. Res.*

2011, *26* (17), 2142–2156.

(70) Stringfellow, G. B. The Role of Impurities in III/V Semiconductors Grown by Organometallic Vapour Phase Epitaxy. *J. Cryst. Growth* **1986**, *75*, 91–100.

(71) Schmid, H.; Björk, M. T.; Knoch, J.; Karg, S.; Riel, H.; Riess, W. Doping Limits of Grown in Situ Doped Silicon Nanowires Using Phosphine. *Nano Lett.* **2009**, *9* (1), 173–177.

(72) Sutter, E.; Sutter, P. Vapor-Liquid-Solid Growth and Sb Doping of Ge Nanowires from a Liquid Au-Sb-Ge Ternary Alloy. *Appl. Phys. A Mater. Sci. Process.* **2010**, *99* (1), 217–221.

(73) Dufouleur, J.; Colombo, C.; Garma, T.; Ketterer, B.; Uccelli, E.; Nicotra, M.; Fontcuberta I Morral, A. P-Doping Mechanisms in Catalyst-Free Gallium Arsenide Nanowires. *Nano Lett.* **2010**, *10* (5), 1734–1740.

(74) Xie, P.; Hu, Y.; Fang, Y.; Huang, J.; Lieber, C. M. Diameter-Dependent Dopant Location in Silicon and Germanium Nanowires. *Proc. Natl. Acad. Sci.* **2009**, *106* (36), 15254–15258.

(75) Li, F.; Nellist, P. D.; Cockayne, D. J. H. Doping-Dependent Nanofaceting on Silicon Nanowire Surfaces. *Appl. Phys. Lett.* **2009**, *94* (26).

(76) Lauhon, L. J.; Gudlksen, M. S.; Wang, D.; Lieber, C. M. Epitaxial Core – Shell and Core – Multishell Nanowire Heterostructures. *Nature* **2002**, *1331* (2001), 57–61.

(77) Tutuc, E.; Guha, S.; Chu, J. O. Morphology of Germanium Nanowires Grown in Presence of B2H6. *Appl. Phys. Lett.* **2006**, *88* (4), 1–3.

(78) Borgström, M. T.; Wallentin, J.; Trägårdh, J.; Ramvall, P.; Ek, M.; Wallenberg, L. R.; Samuelson, L.; Deppert, K. In Situ Etching for Total Control over Axial and Radial Nanowire Growth. *Nano Res.* **2010**, 1–7.

(79) Guilloy, K.; Pauc, N.; Gentile, P.; Robin, E.; Calvo, V. Uniform Phosphorus Doping of Untapered Germanium Nanowires. *Nanotechnology* **2016**, *27*, 485701.

(80) Hochbaum, A. I.; Fan, R.; He, R. R.; Yang, P. D. Controlled Growth of Si Nanowire Arrays for Device Integration. *Nano Lett.* **2005**, *5* (3), 457–460.

(81) Kendrick, C.; Kuo, M. W.; Li, J.; Shen, H.; Mayer, T. S.; Redwing, J. M. Uniform P-Type Doping of Silicon Nanowires Synthesized via Vapor-Liquid-Solid Growth with Silicon Tetrachloride. *J. Appl. Phys.* **2017**, *122* (23).

(82) Schmid, H.; Björk, M. T.; Knoch, J.; Riel, H.; Riess, W.; Rice, P.; Topuria, T. Patterned Epitaxial Vapor-Liquid-Solid Growth of Silicon Nanowires on Si(111) Using Silane. *J. Appl. Phys.* **2008**, *103* (2), 1–7.

(83) Nimmatoori, P.; Zhang, Q.; Dickey, E. C.; Redwing, J. M. Suppression of the Vapor–Liquid–Solid Growth of Silicon Nanowires by Antimony Addition. *Nanotechnology* **2009**, *20* (2), 025607.

(84) Biswas, S.; O'Regan, C.; Petkov, N.; Morris, M. A.; Holmes, J. D. Manipulating the Growth Kinetics of Vapor-Liquid-Solid Propagated Ge Nanowires. *Nano Lett.* **2013**, *13* (9), 4044–4052.

(85) Schmidt, V.; Senz, S.; Gösele, U. Diameter Dependence of the Growth Velocity of Silicon Nanowires Synthesized via the Vapor-Liquid-Solid Mechanism. *Phys. Rev. B - Condens. Matter Mater. Phys.* **2007**, *75* (4), 1–6.

(86) Perea, D. E.; Hemesath, E. R.; Schwalbach, E. J.; Lensch-Falk, J. L.; Voorhees, P. W.; Lauhon, L. J. Direct Measurement of Dopant Distribution in an Individual Vapour-Liquid-Solid Nanowire. *Nat. Nanotechnol.* **2009**, *4* (5), 315–319.

(87) Algra, R. E.; Verheijen, M. A.; Borgström, M. T.; Feiner, L.-F.; Immink, G.; van Enckevort, W. J. P.; Vlieg, E.; Bakkers, E. P. A. M. Twinning Superlattices in Indium Phosphide Nanowires. *Nature* **2008**, *456* (7220), 369–372.

(88) Wallentin, J.; Mergenthaler, K.; Ek, M.; Wallenberg, L. R.; Samuelson, L.; Deppert, K.; Pistol, M.; Borgstr, M. T. Highly Doped InP Nanowires. *Nano Lett.* **2011**, *11*, 2286–2290.

(89) Borgström, M. T.; Norberg, E.; Wickert, P.; Nilsson, H. A.; Trägårdh, J.; Dick, K. A.; Statkute, G.; Ramvall, P.; Deppert, K.; Samuelson, L. Precursor Evaluation for in Situ InP Nanowire Doping. *Nanotechnology* **2008**, *19* (44).

(90) Heitsch, A. T.; Fanfair, D. D.; Tuan, H. Y.; Korgel, B. A. Solution-Liquid-Solid

(SLS) Growth of Silicon Nanowires. *J. Am. Chem. Soc.* **2008**, *130* (16), 5436–5437.

(91) Moutanabbir, O.; Isheim, D.; Blumtritt, H.; Senz, S.; Pippel, E.; Seidman, D. N. Colossal Injection of Catalyst Atoms into Silicon Nanowires. *Nature* **2013**, *496* (7443), 78–82.

(92) Seifner, M. S.; Sistani, M.; Porrati, F.; Di Prima, G.; Pertl, P.; Huth, M.; Lugstein, A.; Barth, S. Direct Synthesis of Hyperdoped Germanium Nanowires. *ACS Nano* **2018**, *12* (2), 1236–1241.

(93) Fukata, N.; Sato, K.; Mitome, M.; Bando, Y.; Sekiguchi, T.; Kirkham, M.; Hong, J. Il; Wang, Z. L.; Snyder, R. L. Doping and Raman Characterization of Boron and Phosphorus Atoms in Germanium Nanowires. *ACS Nano* **2010**, *4* (7), 3807–3816.

(94) Mohite, A. D.; Perea, D. E.; Singh, S.; Dayeh, S. A.; Campbell, I. H.; Picraux, S. T.; Htoon, H. Highly Efficient Charge Separation and Collection across in Situ Doped Axial VLS-Grown Si Nanowire p-n Junctions. *Nano Lett.* **2012**, *12* (4), 1965–1971.

(95) Le, S. T.; Jannaty, P.; Zaslavsky, A.; Dayeh, S. A.; Picraux, S. T. Growth, Electrical Rectification, and Gate Control in Axial in Situ Doped p-n Junction Germanium Nanowires. *Appl. Phys. Lett.* **2010**, *96* (26), 262102.

(96) Le, S. T.; Jannaty, P.; Zaslavsky, A.; Dayeh, S. A.; Picraux, S. T. Growth, Electrical Rectification, and Gate Control in Axial in Situ Doped p-n Junction Germanium Nanowires. *Appl. Phys. Lett.* **2010**, *96* (26), 1–4.

(97) Christesen, J. D.; Pinion, C. W.; Grumstrup, E. M.; Papanikolas, J. M.; Cahoon, J. F. Synthetically Encoding 10-Nm Morphology in Silicon Nanowires. *Nano Lett.* **2013**, *13* (12), 6281–6286.

(98) Chockla, A. M.; Klavetter, K. C.; Mullins, C. B.; Korgel, B. A. Solution-Grown Germanium Nanowire Anodes for Lithium-Ion Batteries. *ACS Appl. Mater. Interfaces* **2012**, *4* (9), 4658–4664.

(99) Lu, X.; Fanfair, D. D.; Johnston, K. P.; Korgel, B. A. High Yield Solution−Liquid−Solid Synthesis of Germanium Nanowires. *J. Am. Chem. Soc.* **2005**, *127* (45), 15718–15719.

(100) He, L.; Xiong, B.; Zhou, P.; Luo, W.; Song, P.; Wang, X.; Hao, Z.; Yang, X.; Niu, C.; Tian, X.; Mengyu, Y.; Liqiang, M. P-Doped Germanium Nanowires with Fano-Broadening in Raman Spectrum. *J. Wuhan Univ. Technol. Mater. Sci. Ed.* **2016**, *31* (1), 52–57.

(101) Storm, K.; Halvardsson, F.; Heurlin, M.; Lindgren, D.; Gustafsson, A.; Wu, P. M.; Monemar, B.; Samuelson, L. Spatially Resolved Hall Effect Measurement in a Single Semiconductor Nanowire. *Nat. Nanotechnol.* **2012**, *7* (11), 718–722.

(102) Park, H.; Beresford, R.; Hong, S.; Xu, J. Geometry- and Size-Dependence of Electrical Properties of Metal Contacts on Semiconducting Nanowires. *J. Appl. Phys.* **2010**, *108* (9).

(103) Yi, C.; Zhaohui, Z.; Deli, W.; Wang, W. U.; Lieber, C. M. High Performance Silicon Nanowire Field Effect Transistors. *Nano Lett.* **2003**, *3* (2), 149–152.

(104) Zheng, G.; Lu, W.; Jin, S.; Lieber, C. M. Synthesis and Fabrication of High-Performance n-Type Silicon Nanowire Transistors. *Adv. Mater.* **2004**, *16* (21), 1890–1893.

(105) Wang, D.; Wang, Q.; Javey, A.; Tu, R.; Dai, H.; Kim, H.; McIntyre, P. C.; Krishnamohan, T.; Saraswat, K. C. Germanium Nanowire Field-Effect Transistors with SiO_2 and High-κ HfO_2 Gate Dielectrics. *Appl. Phys. Lett.* **2003**, *83* (12), 2432–2434.

(106) Hayden, O.; Björk, M. T.; Schmid, H.; Riel, H.; Drechsler, U.; Karg, S. F.; Lörtscher, E.; Riess, W. Fully Depleted Nanowire Field-Effect Transistor in Inversion Mode. *Small* **2007**, *3* (2), 230–234.

(107) Cohen, G. M.; Rooks, M. J.; Chu, J. O.; Laux, S. E.; Solomon, P. M.; Ott, J. A.; Miller, R. J.; Haensch, W. Nanowire Metal-Oxide-Semiconductor Field Effect Transistor with Doped Epitaxial Contacts for Source and Drain. *Appl. Phys. Lett.* **2007**, *90* (23), 23–26.

(108) Tu, R.; Zhang, L.; Nishi, Y.; Dai, H. Measuring the Capacitance of Individual Semiconductor Nanowires for Carrier Mobility Assessment. *Nano Lett.* **2007**, *7* (6),

1561–1565.

(109) Karlström, O.; Wacker, A.; Nilsson, K.; Astromskas, G.; Roddaro, S.; Samuelson, L.; Wernersson, L.-E. Analysing the Capacitance-Voltage Measurements of Vertical Wrapped-Gated Nanowires. *Nanotechnology* **2008**, *19* (43), 435201.

(110) Bakkers, E. P.; van Dam, J. A.; De Franceschi, S.; Kouwenhoven, L. P.; Kaiser, M.; Verheijen, M.; Wondergem, H.; van der Sluis, P. Epitaxial Growth of InP Nanowires on Germanium. *Nat. Mater.* **2004**, *3* (11), 769–773.

(111) Kawashima, T.; Imamura, G.; Saitoh, T.; Komori, K.; Fujii, M.; Hayashi, S. Raman Scattering Studies of Electrically Active Impurities in in Situ B-Doped Silicon Nanowires: Effects of Annealing and Oxidation. *J. Phys. Chem. C* **2007**, *111* (42), 15160–15165.

(112) Kroner, M.; Govorov, A. O.; Remi, S.; Biedermann, B.; Seidl, S.; Badolato, A.; Petroff, P. M.; Zhang, W.; Barbour, R.; Gerardot, B. D.; et al. The Nonlinear Fano Effect. *Nature* **2008**, *451* (7176), 311–314.

(113) Fano, U. Effects of Configuration Interaction on Intensities and Phase Shifts. *Phys. Rev.* **1961**, *124* (6), 1866–1878.

(114) Olego, D.; Cardona, M. Self-Energy Effects of the Optical Phonons of Heavily Doped. *Phys. Rev. B* **1981**, *23* (12), 6592–6602.

(115) Fukata, N.; Chen, J.; Sekiguchi, T.; Matsushita, S.; Oshima, T.; Uchida, N.; Murakami, K.; Tsurui, T.; Ito, S. Phosphorus Doping and Hydrogen Passivation of Donors and Defects in Silicon Nanowires Synthesized by Laser Ablation. *Appl. Phys. Lett.* **2007**, *90* (15), 93–96.

(116) Fukata, N. Doping and Characterization of Impurity Atoms in Si and Ge Nanowires. *Phys. Status Solidi C.* **2014**, *11* (2), 320–330.

(117) Koelling, S.; Li, A.; Cavalli, A.; Assali, S.; Car, D.; Gazibegovic, S.; Bakkers, E. P. A. M.; Koenraad, P. M. Atom-by-Atom Analysis of Semiconductor Nanowires with Parts Per Million Sensitivity. *Nano Lett.* **2017**, *17* (2), 599–605.

(118) Kelly, T. F.; Miller, M. K. Atom Probe Tomography. *Rev. Sci. Instrum.* **2007**, *78* (3),

031101.

(119) He, S. T.; Xie, S. S.; Yao, J. N.; Gao, H. J.; Pang, S. J. Self-Assembled Two-Dimensional Superlattice of Au-Ag Alloy Nanocrystals. *Appl. Phys. Lett.* **2002**, *81* (1), 150–152.

(120) Kamins, T. I.; Li, X.; Williams, R. S.; Liu, X. Growth and Structure of Chemically Vapor Deposited Ge Nanowires on Si Substrates. *Nano Lett.* **2004**, *4* (3), 503–506.

(121) Lauhon, L. J.; Gudiksen, M. S.; Wang, D.; Lieber, C. M. Epitaxial Core – Shell and Core – Multishell Nanowire Heterostructures *Nature* **2002**, *420* (6911), 57–61.

(122) Xiea, P.; Hua, Y.; Fangb, Y.; Huang, J.; Lieber, C. M. Diameter-Dependent Dopant Location in Silicon and Germanium Nanowires. **2017**, *106* (36), 15254–15258.

(123) Wang, F.; Zhou, X.; Zhou, J.; Sham, T. K.; Ding, Z. Observation of Single Tin Dioxide Nanoribbons by Confocal Raman Microspectroscopy. *J. Phys. Chem. C* **2007**, *111* (51), 18839–18843.

(124) Mcguire, K.; Pan, Z. W.; Wang, Z. L.; Milkie, D.; Menéndez, J.; Rao, A. M. Raman Studies of Semiconducting Oxide Nanobelts. *J. Nanosci. Nanotechnol.* **2002**, *2* (5), 499–502.

(125) Zaima, S.; Nakatsuka, O.; Taoka, N.; Kurosawa, M.; Takeuchi, W.; Sakashita, M. Growth and Applications of GeSn-Related Group-IV Semiconductor Materials. *Sci. Technol. Adv. Mater.* **2015**, *16* (4), 43502.

(126) Cristiano, F.; Shayesteh, M.; Duffy, R.; Huet, K.; Mazzamuto, F.; Qiu, Y.; Quillec, M.; Henrichsen, H. H.; Nielsen, P. F.; Petersen, D. H.; et al. Defect Evolution and Dopant Activation in Laser Annealed Si and Ge. *Mater. Sci. Semicond. Process.* **2016**, *42*, 188–195.

(127) Severac, F.; Cristiano, F.; Bedel-Pereira, E.; Fazzini, P. F.; Boucher, J.; Lerch, W.; Hamm, S. Influence of Boron-Interstitials Clusters on Hole Mobility Degradation in High Dose Boron-Implanted Ultrashallow Junctions. *J. Appl. Phys.* **2010**, *107* (12).

(128) Colli, A.; Fasoli, A.; Ronning, C.; Pisana, S.; Piscanec, S.; Ferrari, A. C. Ion Beam Doping of Silicon Nanowires. *Nano Lett.* **2008**, *8* (8), 2188–2193.